A&A, 697, A225 (2025)
https://doi.org/10.1051/0004-6361/202347056

Astronomy & Astrophysics

The CARMENES search for exoplanets around M dwarfs

Cluster analysis of signals from spectral activity indicators to search for shared periods

J. Kemmer[1], M. Lafarga[2,3,⋆], B. Fuhrmeister[4], Y. Shan[5,6], P. Schöfer[7,6], S. V. Jeffers[8], J. A. Caballero[9], A. Quirrenbach[1], P. J. Amado[7], A. Reiners[6], I. Ribas[10,11], V. J. S. Béjar[12,13], F. Del Sordo[10,11], A. P. Hatzes[8], Th. Henning[14], I. Hermelo[15], A. Kaminski[1], D. Montes[16], J. C. Morales[10,11], and S. Reffert[1]

[1] Landessternwarte, Zentrum für Astronomie der Universität Heidelberg, Königstuhl 12, 69117 Heidelberg, Germany
[2] Department of Physics, University of Warwick, Gibbet Hill Road, Coventry CV4 7AL, UK
[3] Centre for Exoplanets and Habitability, University of Warwick, Coventry CV4 7AL, UK
[4] Hamburger Sternwarte, Gojenbergsweg 112, 21029 Hamburg, Germany
[5] Centre for Earth Evolution and Dynamics, Department of Geosciences, Universitetet i Oslo, Sem Sælands vei 2b, 0315 Oslo, Norway
[6] Institut für Astrophysik, Georg-August-Universität, Friedrich-Hund-Platz 1, 37077 Göttingen, Germany
[7] Instituto de Astrofísica de Andalucía (IAA-CSIC), Glorieta de la Astronomía s/n, 18008 Granada, Spain
[8] Thüringer Landessternwarte Tautenburg, Sternwarte 5, 07778 Tautenburg, Germany
[9] Centro de Astrobiología (CAB, CSIC-INTA), Camino Bajo del Castillo s/n, Campus ESAC, 28692 Villanueva de la Cañada, Madrid, Spain
[10] Institut de Ciències de l'Espai (ICE, CSIC), c/ de Can Magrans s/n, Campus UAB, 08193 Cerdanyola del Vallès, Spain
[11] Institut d'Estudis Espacials de Catalunya (IEEC), c/ Gran Capità 2–4, 08034 Barcelona, Spain
[12] Instituto de Astrofísica de Canarias (IAC), 38205 La Laguna, Tenerife, Spain
[13] Departamento de Astrofísica, Universidad de La Laguna, 38206 La Laguna, Tenerife, Spain
[14] Max-Planck-Institut für Astronomie, Königstuhl 17, 69117 Heidelberg, Germany
[15] Centro Astronómico Hispano en Andalucía, Observatorio de Calar Alto, Sierra de los Filabres, 04550 Gérgal, Spain
[16] Departamento de Física de la Tierra y Astrofísica & IPARCOS-UCM (Instituto de Física de Partículas y del Cosmos de la UCM), Facultad de Ciencias Físicas, Universidad Complutense de Madrid, 28040 Madrid, Spain

Received 30 May 2023 / Accepted 26 February 2025

ABSTRACT

Context. A multitude of spectral activity indicators are routinely computed nowadays from the spectra generated as part of planet-hunting radial velocity surveys. Searching for shared periods among them can help to robustly identify astrophysical quantities of interest, such as the stellar rotation period. However, this identification can be complicated due to the fact that many different peaks occur in the periodograms. This is especially true in the presence of aliasing and spurious signals caused by environmental influences affecting the instrument.

Aims. Our goal is to test a clustering algorithm to find signals with the same periodicity, (i.e. with the stellar rotation period) in the periodograms of a large number of activity indicators. On this basis, we have looked to evaluate the correlations between activity indicators and fundamental stellar parameters.

Methods. We used generalised Lomb–Scargle periodograms to find periodic signals in 24 activity indicators, spanning the VIS and NIR channels of the CARMENES spectrograph. Common periods were subsequently determined by a machine learning algorithm for density-based spatial clustering of applications with noise (`DBSCAN`).

Results. The clustering analysis of the signals apparent in the spectral activity indicators is a powerful tool for the detection of stellar rotation periods. It is straightforward to implement and can be easily automated, so that large data sets can be analysed. For a sample of 136 stars, we were able to recover the stellar rotation period in a total of 59 cases, including 3 with a previously unknown rotation period. In addition, we analysed spurious signals frequently occurring at the period of one year and its integer fractions, concluding that they are likely aliases of one underlying signal. Furthermore, we reproduced the results of several previous studies on the relationships between activity indicators and the stellar characteristics.

Key words. techniques: radial velocities – stars: activity – stars: late-type – stars: low-mass – stars: rotation

1. Introduction

The intrinsic variability of stars that possess an outer convective zone is one of the main challenges in detecting and characterising exoplanets orbiting cool stars with high-resolution spectroscopy. The presence of magnetic activity features on the stellar surface, such as cool spots, hot faculae, or surface granulation, distort the symmetrical shape of the absorption line profiles used to measure radial velocities (RVs). As a result, a true Doppler shift could end up hidden due to an orbiting planet

⋆ Corresponding author.

(e.g. Desort et al. 2007; Barnes et al. 2011; Liebing et al. 2021; Jeffers et al. 2022) or end up recorded as a false-positive planet (e.g. Queloz et al. 2001; Desidera et al. 2004; Huélamo et al. 2008; Figueira et al. 2010; Hatzes 2013; Rajpaul et al. 2016; Haywood et al. 2014; Santos et al. 2014; Robertson et al. 2015, among many examples). Stellar activity features such as starspots can have lifetimes longer than the stellar rotation period and their impact on the RVs could be coincident with the stellar rotation period (e.g. Boisse et al. 2011; Haywood et al. 2014; Rajpaul et al. 2015; Stock et al. 2020a,b; Kossakowski et al. 2022). Stars also display long-term magnetic cycles that change their overall activity level (e.g. Gomes da Silva et al. 2011; Brandenburg et al. 2017; Díez Alonso et al. 2019; Terrien et al. 2022; Jeffers et al. 2023; Fuhrmeister et al. 2023).

Several indicators of stellar activity are often used to estimate stellar rotation periods and long-term cycles, as well as to disentangle stellar-induced RVs signals from those induced by true planetary companions. These include photometric time series that measure brightness variations on the stellar surface, as well as time series of spectroscopic indicators derived from the same data used to measure RVs (e.g. Queloz et al. 2001; Boisse et al. 2009; Astudillo-Defru et al. 2017b; Kemmer et al. 2022). Common spectroscopic activity indicators include measurements of excess emission flux in the core of chromospheric lines (e.g. Wilson 1968; Baliunas et al. 1995; West et al. 2004; Houdebine et al. 2009; Jeffers et al. 2018; Schöfer et al. 2019), the strength of photospheric bands (e.g. Berdyugina & Solanki 2002; Lépine et al. 2007; Schöfer et al. 2019), indicators tracing average shape changes in absorption lines such as those derived from the cross-correlation function (CCF) or template matching approaches (e.g. Queloz et al. 2001; Gomes da Silva et al. 2012; Lafarga et al. 2020; Barnes et al. 2024), or wavelength-dependent RV changes traced by the chromatic index (CRX; Zechmeister et al. 2018; Tal-Or et al. 2018; Jeffers et al. 2022; Jeffers et al. 2025). Furthermore, magnetic field proxies derived from polarimetric measurements can also be used as activity indicators (e.g. Fouqué et al. 2023).

Several works have studied the temporal behaviour of activity indicators in cool stars, and how they relate to each other as well as to the RV measurements (e.g. Martínez-Arnáiz et al. 2010; Lovis et al. 2011; Robertson et al. 2013; Suárez Mascareño et al. 2015, 2017, 2018; Mignon et al. 2023). However, we still do not have a clear picture of how different indicators behave with respect to different types of stars. In this work, we focus on M dwarf stars observed within the CARMENES survey (Quirrenbach et al. 2014; Ribas et al. 2023), a sample that spans all M dwarf sub-spectral types with varying average activity levels. Alongside the search for exoplanets, studying the activity of M dwarfs has always been a central interest of the CARMENES survey. A number of studies have previously investigated the sensitivity to activity of spectroscopic indicators in the wavelength range of CARMENES. Tal-Or et al. (2018) found correlations between RV and CRX for about a third of stars in a sample of ∼30 stars showing large RV scatter. Schöfer et al. (2019) studied the temporal variability of chromospheric indicators and photospheric absorption band indices in the CARMENES sample (composed of 331 M dwarfs at the time). Out of 133 stars with known stellar rotation period longer than 1 day, this study identified 15 stars with a significant periodic signal related to the rotation period in more than two indicators. The authors found that the indicators most likely to vary with the rotation period were the TiO λ7048 Å and TiO λ8428 Å photospheric band indices, along with the Hα and the Ca IRT$_b$ indices. In a subsequent work, Schöfer et al. (2022) focussed on an in-depth study of four stars with different activity levels and sub-spectral types. The authors found that RVs and photospheric indicators (especially the TiO λ7048 Å index) clearly vary with the stellar rotation period, while chromospheric indicators only show clear signals for low activity levels. Moreover, the authors also observed changes over time in the dominant harmonic, that is, episodes in which indicators vary with the rotation period and other episodes where they vary with half the rotation period. Lafarga et al. (2021) studied a sub-sample of 98 stars and found that indicators behave differently depending on the mass and activity level of the stars. The authors found activity-related periodic signals in 56 stars of the sample in various indicators. Stars with low activity levels tend to show signals in chromospheric indicators, while indicators such as CRX and CCF bisector inverse slope (CCF-BIS) show signals in the high-activity regime. Most stars show a signal related to the rotation period in the RVs and about half of them showed signals in the differential line width (dLW) and CCF full width at half maximum (CCF-FWHM), especially fully convective M dwarfs.

Fuhrmeister et al. (2019) presented a comparison of different methods to search for long-term periodic signals or cycles in the time-series of CARMENES activity indicators. They investigated the variability of the Hα, Na I doublet, and Ca II IRT indices for 16 stars and found that Gaussian process regression and the classical periodogram analysis provide the best results.

However, all these studies were focussed on individual lines and partial aspects of the properties and behaviour of the activity indicators, as such detailed evaluations are not feasible on a large basis in a meaningful way. This is mainly due to the large number of spectroscopic activity indicators, which can have different sensitivities to rotational periods and can be related to stellar properties in complex ways. Furthermore, the interpretation of the multitude of signals in the time series of the indicators, including the need to filter out contamination by non-astrophysical signals, is non-trivial. Meanwhile, machine learning techniques provide promising ways to tease out meaningful signals from large collections of data. Clustering algorithms, for instance, are often used to find groups with similar properties. A prominent example is the detection of star clusters in the data of astrometric satellite missions (e.g. Caballero & Dinis 2008; Castro-Ginard et al. 2018; Hunt & Reffert 2021). In this work, we used the density-based spatial clustering of applications with noise (`DBSCAN`; Ester et al. 1996) to detect signals that coincidentally occur in the periodograms of time series of several stellar activity indicators. In doing so, we took advantage of the fact that although each individual indicator may hold an ambiguous significance for a particular star, analysing a set of indicators can reveal patterns that help identify activity related signals, such as the stellar rotation period or long-term trends, as well as common spurious signals. The analysis is based on an updated data set from the CARMENES survey, which includes the full set of routinely computed activity indicators for all stars in the survey.

The paper is structured as follows. In Sect. 2, we give an overview on the stellar sample and spectral activity indicators that we analyse. Our methods and the procedure to determine the clusters of signals in the indicators are described in Sect. 3. The results from the application of the clustering algorithm for the robust detection of stellar rotation periods and activity cycles are presented and discussed in Sects. 4 and 5. Finally, we highlight our conclusions in Sect. 6.

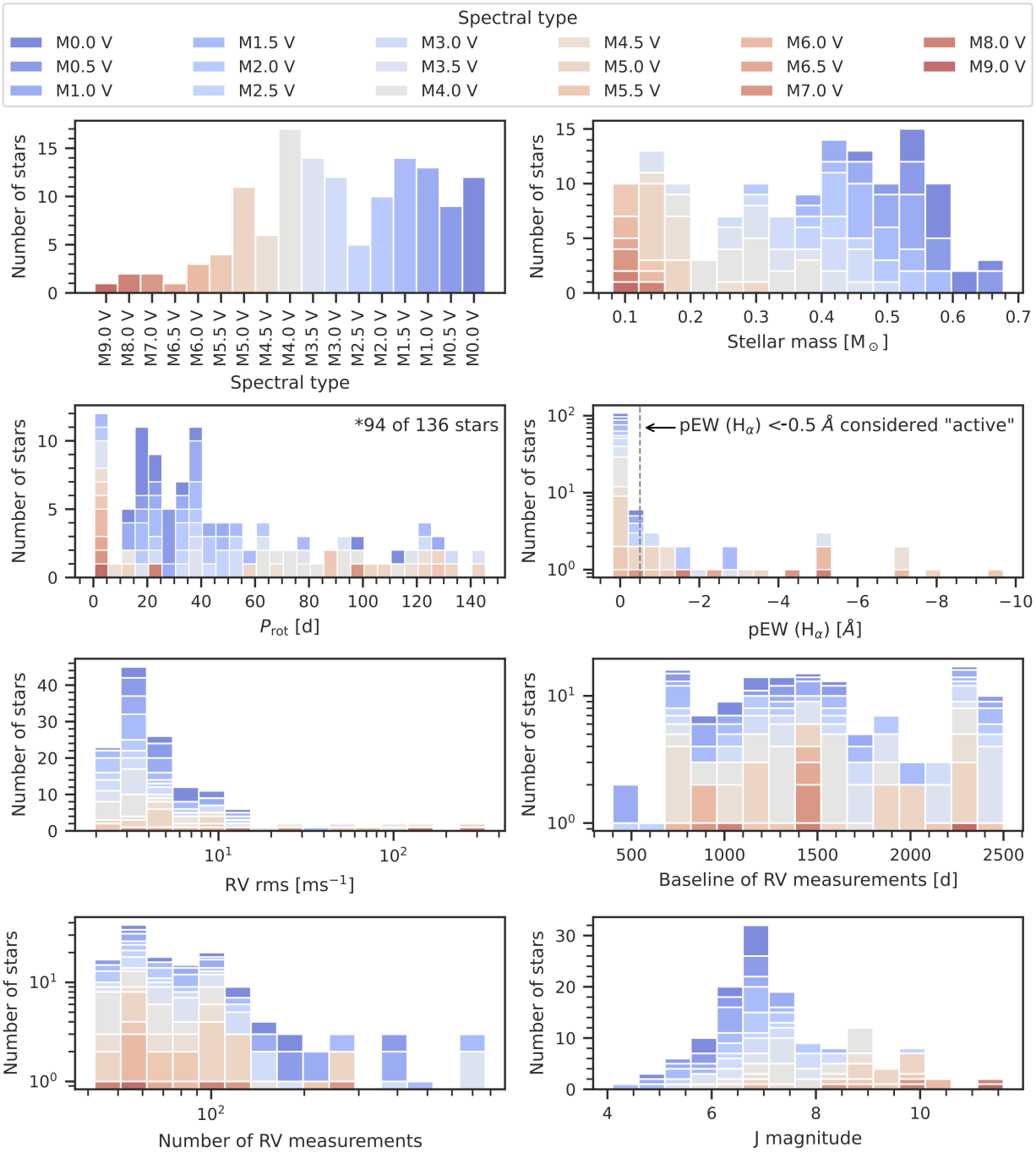

Fig. 1. Overview on the properties of the stellar sample.

2. Data

2.1. Stellar sample

Our analysis was based on 362 stars from the CARMENES sample of M dwarfs (Quirrenbach et al. 2016; Reiners et al. 2018b; Ribas et al. 2023). We used observations taken between January 2016 and November 2022 as part of the guaranteed time observations and the legacy project of CARMENES. To ensure an adequate sampling, we selected for our analysis only M dwarfs from the CARMENES sample that had a minimum number of 40 observations over a period of at least one year. Furthermore, we excluded data with large gaps of more than 40% of the time of the observations, as these gaps can lead to severe aliasing. As in Lafarga et al. (2021) and Fuhrmeister et al. (2023), we also removed all binary stars from the sample that were identified by Baroch et al. (2018) and Baroch et al. (2021). The resulting final sample consists of more than 14 000 spectra from 136 stars, out of which 97 have a known stellar rotation period (Shan et al. 2024). We show an overview of various key properties of the sample in Fig. 1.

2.2. Spectral activity indicators

The advantage of using CARMENES spectra to analyse stellar activity indicators is its broad wavelength range. There are 24 activity indicators covered by the VIS and NIR channels of

CARMENES as listed in Table A.1. As outlined in the introduction, their sensitivity to stellar activity of M dwarfs and their predictive power for the stellar rotation period have already been investigated in detail in several studies of the CARMENES consortium (see Table A.1 for a list of relevant references). Generally, the indicators can be divided into three different categories: (*i*) chromospheric line indicators: the largest category, which includes Hα, for which line indices (Zechmeister et al. 2018) or (pseudo-)equivalent-widths (pEW, Schöfer et al. 2019) can be determined for our M-dwarf stars; (*ii*) photospheric absorption band indices: For broader photospheric lines, such as the TiO lines, no (pseudo-)continuum can be determined, so we used band indices instead (Schöfer et al. 2019); and (*iii*) broad spectrum diagnostics: In addition, there are a number of indicators that are diagnostic to the whole spectrum (hereafter diagnostic indicators). These include the RV measurements themselves, as well as the CCF parameters (Lafarga et al. 2020) and dLW (Zechmeister et al. 2018), which are sensitive to changes in the shape of the spectral lines caused by activity. Furthermore, there is CRX (Zechmeister et al. 2018), which expresses the wavelength dependence of the measured RVs.

We present an overview of all the activity indicators analysed in this work and the references for the methods used to calculate them in Table A.1. We note that there are different definitions of the line indices in the presented literature. However, these differences do not have a major impact on our results since we are only interested in periodic signals in each of them individually and do not compare their absolute values (Fuhrmeister et al. 2019).

3. Analysis

3.1. Periodogram analysis

3.1.1. Method

For our periodogram analysis, we used the `astropy` (Astropy Collaboration 2018) implementation of the generalised Lomb-Scargle (GLS) periodogram normalised to unity (Zechmeister & Kürster 2009) with an oversampling factor of ten to properly resolve the peaks (VanderPlas 2018). Our periodogram analysis considered formal uncertainties of the activity indicators, thereby accounting for differences in quality of the spectra used to calculate them (i.e. signal-to-noise ratio of the spectra, influences from flares, etc.). The false alarm probabilities (FAPs) were calculated using the analytic expression of Baluev (2008).

There are two different approaches to identify the signals from the periodograms. The naive method is to create the periodogram and note down the periods of all visible peaks above a given FAP threshold. However, because the GLS periodogram only considers one period at a time, dominant signals can completely suppress lower amplitude signals that may be missed in this way. A more sophisticated approach is to perform an iterative pre-whitening of the data, as is usually done when searching for planets in RV data. We performed this pre-whitening by generating the periodogram and finding the period with the lowest FAP. Next, the sinusoidal model corresponding to the signal was subtracted from the data and a new periodogram was generated from the residuals. The process was then repeated until no more signals above the specified FAP threshold were detected.

An effect of the pre-whitening method is that it also removes alias peaks occurring in the periodogram. This removal has pros and cons for the clustering algorithm (Sect. 3.2). The advantage is that it significantly reduces false-positive clusters and crowding at the alias periods of the signals present in the data. On the other hand, the true underlying period creating the aliases does not always have the highest power in the periodogram (Dawson & Fabrycky 2010; VanderPlas 2018). If during the pre-whitening an alias of the true period is removed (instead of removing the true period), this leads to a loss of data points in the cluster corresponding to the correct period, which may cause the clustering algorithm to miss it.

In the top two panels of Fig. 2, we show as an example the results from the clustering algorithm obtained using the two different approaches to determine the signals from the periodograms. Because the aliases have been removed by the pre-whitening method, significantly fewer clusters were found in that case. The width of the individual clusters in the pre-whitening approach is significantly narrower because the close aliases caused by long-term sampling frequencies in the window function of the data are diminished. For our clustering analysis, we used both approaches: the naive method and the pre-whitening method. We compared their performance regarding the success in detecting the stellar rotation periods.

3.1.2. Signal search

Following Lafarga et al. (2021), we removed outliers and data points with large uncertainties using a sigma clipping with a threshold of $3\,\sigma$ in the absolute values and uncertainties before creating the periodograms. We performed this clipping to exclude observations during stellar flares and, in general, to exclude observations with a poor signal-to-noise ratio (S/N).

The power of long-period signals is often greater in their one-day aliases than in the actual periods (Dawson & Fabrycky 2010). For this reason, we chose a lower bound of 1.5 d for the period range to minimise the impact of the one-day alias and to facilitate an automatic detection of the correct signals. We note that this cut can affect the signal recovery of fast-rotating stars, which tend to be either very young or late-M dwarfs. Very fast rotators comprise a very small fraction of our sample, that is, 4/136 of our targets have a confirmed $P_{\rm rot}$ <1.5 d and they are all late-M dwarfs (Shan et al. 2024, see Table C.1 for details). We note that fast rotator candidates may be identified via spectroscopic $v \sin i$, since $P_{\rm rot}$ =1.5 d corresponds to an equatorial surface rotation velocity of between 3 and 20 km s^{-1} (for late to early M dwarfs). We further note that since very short signals are severely under-sampled with spectroscopic monitoring, methods based on spectroscopic activity indicators are inefficient at detecting very short signal compared to using photometric data. Since young stars tend to be fast rotators, our cut at 1.5 d could also be biasing our period recovery of young stars. We note that it is hard to define a clear cut in period that separates young and old M dwarfs (see e.g. Cortés-Contreras et al. 2024, where the authors find young stars with periods above 2 d, but old, very late M dwarfs with periods below 1 d). According to Cortés-Contreras et al. (2024), none of the four short-period stars mentioned above have been classified as young. Therefore, it remains unclear how our lower period boundary can bias our results regarding the youth of our targets.

By limiting the upper range of the period grid, it is (in principle) possible to improve the power of signals with a potential origin from stellar rotation, as we would expect those to be generally lower than 200 d (e.g. Newton et al. 2016, 2018; Shan et al. 2024). However, in our analysis we were also interested in potential long-term activity cycles, which can, as mentioned above, significantly affect the power of shorter periods. Therefore, we adopted the standard in the GLS implementation from `astropy`,

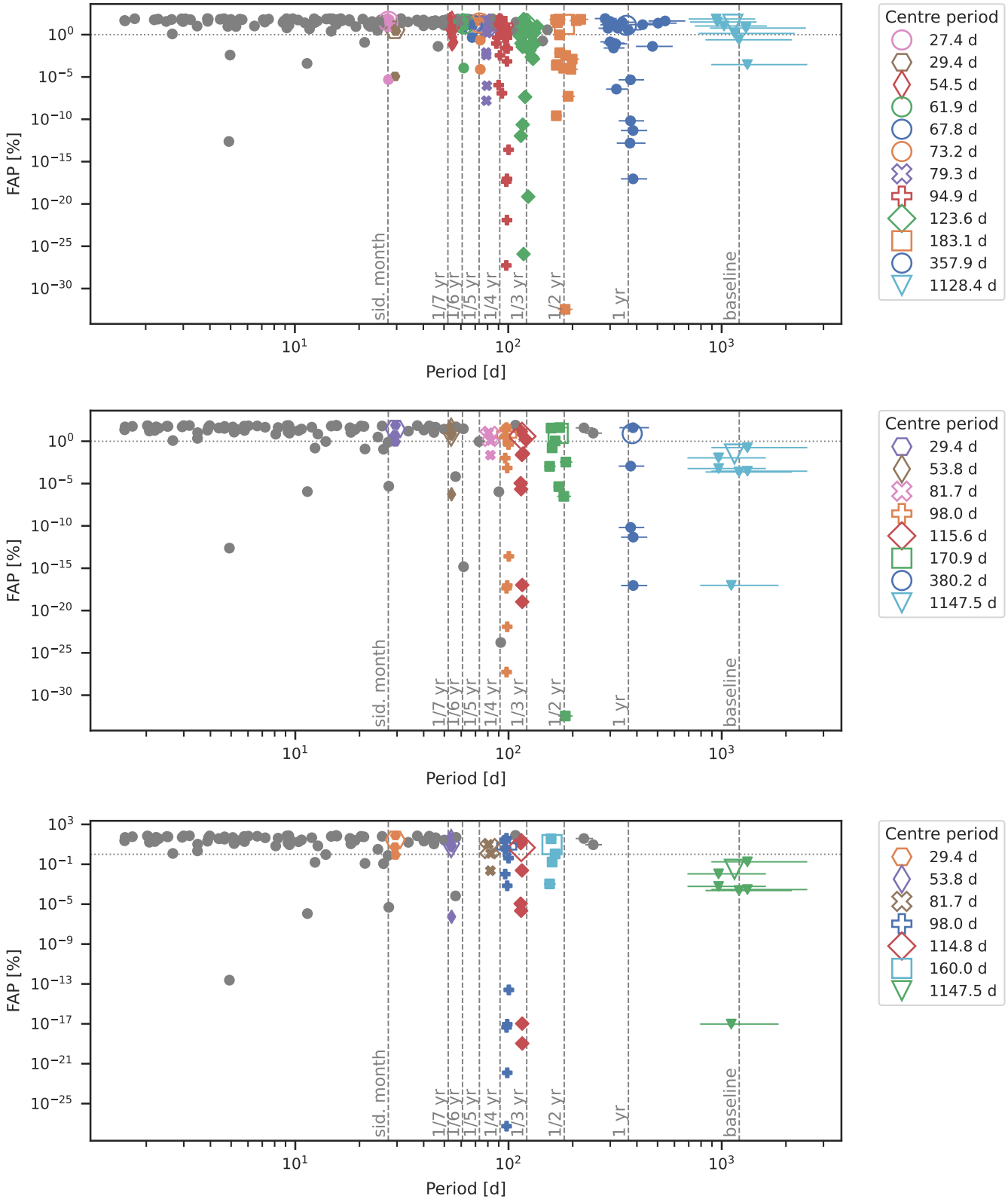

Fig. 2. Results of the clustering algorithm for Teegarden's Star. *Top*: using the naive approach. *Middle*: using the pre-whitening approach. *Bottom*: using pre-whitening and excluding periods close to the harmonics of one year. The coloured filled symbols show the individual data points of the detected clusters, with the error bars corresponding to the peak width in the GLS, and the open symbols yield the mean values of the clusters. Grey dots denote data points that were identified as noise by the clustering algorithm. The colour mapping changes between the plots to emphasise that although there is some overlap, the clusters (and thus technically also the mean periods) that appear change between the different methods. Clusters that are consistent between all plots within the GLS resolution are always denoted by the same non-circular markers. The FAP of 1% is marked by the grey horizontal dotted line and the grey vertical dashed lines show different periods of interest. The baseline indicates the timespan of the observations.

which is two times the timespan of our observations (hereafter baseline) multiplied by the oversampling factor.

An important parameter for the signal search is the FAP threshold, which is usually set between 1% and 0.1% in periodogram analysis. Since the clustering algorithm combines the signals from periodograms of multiple indicators, we took advantage of the fact that the FAP for a cluster of signals to occur at a specific period in multiple periodograms is much lower than the FAP of a single periodogram (see Sect. 7.10.1 in Hatzes 2019). We found that a FAP threshold of $\mathrm{FAP}_{\mathrm{max}} \leq 80\%$ in the individual periodograms provides a good balance between the number of detected spurious signals and the recovery rate of the stellar rotation period, as shown in Sect. 4.1. In cases where the periodograms suffered from severe aliasing, a FAP threshold as the only limit in the signal search led to tens or even hundreds of spurious signals detected. Therefore, we limited the search to no more than 25 detected signals per activity indicator. In this way, summed up over all activity indicators, we detected an average of eight periodic signals per target with the naive approach and three periodic signals through pre-whitening.

3.2. Clustering analysis

3.2.1. Method

To investigate the occurrence of clustering in the periodicities detected in all 24 activity indicators listed in Table A.1, we used the `DBSCAN` algorithm implemented in `scikit-learn` (Pedregosa et al. 2011). Compared to other popular clustering algorithms, it has the advantage that it can also take noise into account (i.e. it is robust to outliers that do not belong to any cluster). This feature is particularly important for our analysis, as many spurious signals emerge from the periodogram analysis due to our low FAP thresholds. The `DBSCAN` algorithm is defined by two parameters: the distance parameter ϵ, which describes the distance between two data points that are to be considered being in a 'neighbourhood' relation and $\mathrm{min}_{\mathrm{data\ points}}$, which is the minimum number of data points required for such a neighbourhood to be considered a cluster. In our case the data points are the measured signals from the periodogram analysis and the distance is the difference in their periods or frequencies. Tuning the ϵ parameter changes the resolution of the clustering algorithm. If it is too large, clusters may be merged, leading to incorrect period estimates. On the other hand, if the ϵ parameter is too small, the clusters may be fragmented, resulting in the loss of data points that are incorrectly marked as outliers. The minimum number of data points basically determines the density of the clusters. However, as we are dealing with a relatively small number of data points, $\mathrm{min}_{\mathrm{data\ points}}$ is (in our context) more a measure of the reliability of a cluster. The more data points in a cluster, the more likely it is that there is a physical reason for the signals to occur at the same period rather than by chance.

3.2.2. Cluster search

We used a one-dimensional (1D) input for the `DBSCAN` method, which represents the frequencies[1] of the signals that we determined for each target in the periodogram analysis of the activity indicators. To be consistent with the signal search, we set the ϵ parameter of the `DBSCAN` algorithm to half of the peak width in the GLS periodograms ($\epsilon = 1/2 \times$ baseline in frequency space). In the classical periodogram analysis, a significant signal in the periodogram of both RVs and a single activity indicator is often reason enough to attribute said signal to stellar activity. For this reason, we kept the required minimum number of data points per cluster small and set it to 3. As a result, a cluster in our analysis corresponds to the agglomeration of at least three signals from the GLS periodograms of different activity indicators, where the difference in frequency to the nearest neighbour is not greater than the resolution of the periodograms. Due to the low FAP threshold in the periodogram analysis, this definition resulted in many spurious clusters consisting only of data points with high FAP. Therefore, we introduced an additional criterion for our analysis, and only considered clusters in which at least one data point meets the classical requirements and has a FAP of less than 1%.

A notable first result was that the clustering of the activity indicators in most cases shows very strong signals around the period of one year and its integer fractions (see the upper panel in Fig. 2). Using the pre-whitening method in the periodogram analysis can remove some of these signals, as they are created by aliasing (middle panel in Fig. 2), but the often very large clusters around the one and half year period are largely unaffected by this pre-whitening. In order to facilitate an automated evaluation to find signals with an activity origin as presented in Sects. 4.1 and 4.2, we therefore removed from the analysis all peaks that were consistent with integer fractions (up to 1/6) of one year within the uncertainties of the GLS before applying the clustering algorithm. An exemplary result for Teegarden's star is shown in the lower panel of Fig. 2.

4. Results

4.1. Detecting the stellar rotation period

4.1.1. An example: Teegarden's Star

The search for the stellar rotation period is the most obvious application of the clustering algorithm of the activity indicators. As an example, we show the results from Teegarden's Star in Fig. 2. Teegarden's Star is host to at least three (approximately) Earth-mass planets, with the inner two in its liquid water habitable zone (Zechmeister et al. 2019; Dreizler et al. 2024). The very low-mass star shows additional RV signals that might be related to stellar activity. It has a spectroscopically determined period of ∼100 d, as seen in several spectroscopic activity indicators (96.2, 97.6, 99.6 d, depending on the indicator and dataset; see Lafarga et al. 2021; Terrien et al. 2022). The large number of clusters that appear in the clustering diagrams in Fig. 2 serves as a good example of the procedure for evaluating the cluster analysis. As described in Sect. 3.2.2, the signals from one year and its integer fractions can interfere with the search for the stellar rotation period (see the top two panels of the figure). Therefore, we focussed on the bottom panel of the figure, where we removed data points from the dataset that were consistent within their uncertainties (i.e. peak width in the GLS) with integer fractions of one year up to 1/6 before applying the clustering algorithm.

The distribution of clusters in the bottom clustering diagram can be explained by three different signals. First, the cluster with the most data points and overall lowest FAP has a period of ∼98 d and is consistent with the rotation periods in the literature. There is an alias of this signal at ∼82 d due to an approximately yearly sampling frequency in the window function of the data. Another cluster at ∼54 d can likely be attributed to the second

[1] So far, we have always referred to the periods, as they are more intuitive. For a better understanding of the actual implementation of the clustering algorithm, however, it is necessary to switch to the frequency domain in Sect. 3.2.2, as this is the natural unit of the periodograms.

harmonic of the presumed rotation period. The period of 29.4 d coincides with the lunar cycle, but is also very close to the third harmonic of the presumed rotation period (see also the analysis of spurious signals in Sect. 4.3). The second-biggest cluster has a period of ∼114 d with an alias at ∼160 d caused by the yearly sampling. This signal could be related to the spurious RV signal at ∼175 d that was already discussed by Zechmeister et al. (2019). Alternatively, it could also be related to the rotation period, since long periods tend to have large uncertainties (Shan et al. 2024). Lastly, there is a third cluster of signals coinciding with the length of the data baseline that corresponds to a long-term trend in the GLS periodograms, and is probably an imprint of a stellar magnetic cycle. Very similar periods were independently found by Fuhrmeister et al. (2024) based only on Hα and classical periodogram analysis.

For completeness, we note here that some indicators (the RV being the most significant one) show peaks close to periods of the three planets orbiting the star (orbital periods of ∼4.9, 11.4, and 26.1 days, for planets b, c, and d, respectively). However, contrary to the other signals discussed above, no significant cluster is observed at any of these periods because these periodicities do not appear in other indicators.

4.1.2. Application to the whole sample

We performed an automated search for the stellar rotation periods on the whole sample and compared the results for the naive and pre-whitening methods from the signal search. We removed the signals close to one year and its integer fractions (up to 1/6; i.e. data points consistent with those within their uncertainties). To determine the stellar rotation period, we defined the most likely period, $P_{\rm rot,cl}$, to correspond to the cluster with the most data points in it that has a period below 200 d. Alternatively, selecting the cluster with the lowest mean FAP as the rotation period did not change our conclusions, nor did taking the cluster with the overall data point with the lowest FAP. The results for the rotation periods determined in this way are listed in Table C.1, together with other key properties of the stars. Additional clusters present in the period range below 200 d, which were not selected as the rotation period, were usually connected to the respective rotation period by aliasing or harmonic relations. Only a few cases showed additional clusters at unrelated periods, which could indicate other forms of stellar variability or spurious signals. However, a detailed analysis of these clusters is beyond the scope of this paper.

Shan et al. (2024) provided a review on the rotation periods of 253 stars from the CARMENES survey, most of which measured from photometric data. For our selected stars, they listed 97 stars with rotation periods, $P_{\rm rot,lit}$, that are either 'secured' or 'tentative' (but likely), which we compared with the results from our period search as presented in Fig. 3. We assumed that it was a match if the difference between the period obtained by the clustering algorithm and the literature value was less than 15% of the literature period. We recovered 36 (38%) of the rotation periods using the naive approach and 42 (45%) using the pre-whitening for the signal search. Taking into account the instances in which the clustering algorithm detected a harmonic or a first-order alias of the literature period (daily or yearly sampling considered), we found additional matches for the periods in 18 cases (57% in total) using the naive approach and in 10 cases (55% in total) using the pre-whitening approach.

The naive method thus appears to detect more rotation-related signals, while the pre-whitening method yields the most direct matches. Furthermore, the two methods differ not only in the number but also in the actual signals that are found. In the naive method, 9 periodicities were detected in stars for which no activity signal was found with the pre-whitening method and, conversely, the pre-whitening method found 7 signals that were not identified with the naive method. Combining both methods, 56 out of 97 stars with known rotation periods were found by the cluster analysis to have activity signals either related to the literature value directly, harmonically, or by aliasing. This combination shows that a careful manual analysis of all clusters that occur, as shown in the previous section for Teegarden's Star, is beneficial.

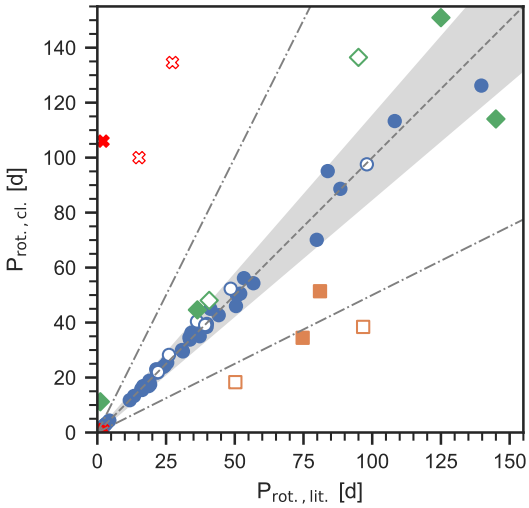

Fig. 3. Comparison between rotation periods determined from the clustering algorithm and literature values. Depicted are the results for the signals found with the pre-whitening method in the periodogram analysis. Rotation periods where we found a direct match are depicted by blue circles. Cases where the period from the clustering algorithm is a harmonic or an alias of the literature period are marked by orange squares and green diamonds, respectively. Red crosses highlight stars where the period from the clustering algorithm has no apparent relation to the literature value. Filled symbols depict confirmed rotation periods, while open symbols depict tentative ones, following Shan et al. (2024). The grey shaded area and dashed line signal a 1-to-1 correlation with a margin of 15% of the value. A harmonic correlation (either double or half of the period) is indicated by the grey dashed-dotted lines.

The biggest difference between the two methods is the number of false-positive detections, namely, the case where a cluster is found, but its period does not match the literature period according to our criteria. The nominal number of false-positives is 19 for the naive method and only 4 for the pre-whitening method. The reason behind this difference is that without pre-whitening, there are often clusters of high order aliases of the period of one year that are not caught by our filtering for the spurious periods (see Sect. 4.3 for a more in-depth investigation of those signals). Given the higher number of direct matches and the lower number of false positives, we therefore proceeded with the results from the pre-whitened signal search in the further analysis.

The majority of the unrecovered literature periods are cases where no clusters of activity indicators were found at all. The false positives occur for stars where the actual period is not present as a cluster, as, for example, in LP 560–035 and/or where the actual rotation period is shorter than 1.5 d – and is therefore outside the range of our signal search; in such cases, spurious signals at longer periods were determined instead. We note

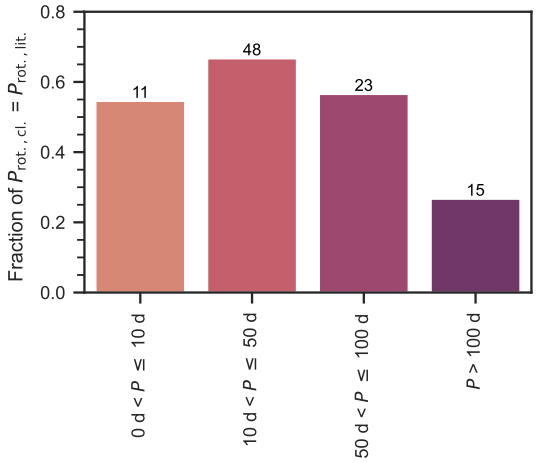

Fig. 4. Fraction of stars for which the literature rotation period was recovered as a function of the rotation period. The number on top of each bar denotes the number of stars with a literature rotation period for each category.

however that for vB 8, with a literature period shorter than 1.5 d, some cluster match a daily alias of the period.

For two additional false positives (G 264–012 and GJ 810 B), the rotation period is 'tentative' according to Shan et al. (2024). Both have long rotation periods ($P \geq 100$ d), which makes the detection inherently more difficult (see the next section and the discussion in Sect. 5). Lastly, HH And displays a cluster of long-term signals ($P > 200$ d; see also Sect. 4.2), which could lead to erroneous signals.

We also examined the three stars for which a cluster was detected, but no rotation period is known in the literature (BD+09 2636, BD-07 3856, and HD 199305; highlighted in bold font in Table C.1). After a visual inspection of the cluster diagrams for each star (see Appendix D), we deemed all of them to be credible detections and therefore publish them as new estimates of the stellar rotation period for those stars. The periods range from 21 d to 160 d, and the stars cover the spectral types M0.5 V to M1.0 V. The period of 160 d determined for HD 199305 seems rather long for such an early M1.0 V star. However, the reliability is rather high having four indicators (He I λ10 830 Å, Ca IRT$_c$, Ca IRT$_b$, dLW) exhibiting FAP lower than 1%. We further checked the phase-folded data of the relevant activity indicators for these three targets. All display a significant periodicity at the reported periods, which reinforces our confidence on the period values.

4.1.3. Relations to the stellar properties

We searched for relations between the signals detected by the clustering algorithm and the stellar properties of our sample. In Fig. 4, we show the recovery rate of the literature period as a function of the stellar rotation period. We had significantly fewer matches for longer rotation periods, as can be expected since stars with longer rotation periods tend to be less active, implying a minor variability amplitude in the indicators (e.g. Reiners et al. 2012; Newton et al. 2017).

The recovery rate as a function of spectral type is difficult to assess because there are few very late-type M dwarfs in the sample (see left panel in Fig. 5). However, when this is taken together with the number of stars for which the clustering algorithm did not yield any clusters (see right panel in Fig. 5), a consistent picture emerges. For both Hα-active and inactive stars, the recovery rate and non-detections display a high success rate for early to mid-M dwarfs, but a noticeable drop for stars of spectral types M3.5 V to M4.0 V. For later spectral types, the results are very mixed due to the small sample size, with both high recovery and non-detection rates. One reason is that five of the stars with spectral types later than M5.5 V have known rotation periods shorter than 1.5 d, which is outside the range of our signal search as described above.

There are other stellar parameters that can be related to our detection of rotation periods. Recently, Cortés-Contreras et al. (2024) studied the kinematics and its connection to rotation period and velocity, X-ray, near-UV, and Hα emission, and magnetic field strength of the whole CARMENES input catalogue, including all our M dwarfs (Alonso-Floriano et al. 2015b; Reiners et al. 2022). From the comparison of the list of stars in their study and for which we searched for a $P_{\mathrm{rot,cl}}$, we concluded that most of our 136 stars are neither very young nor very old. The younger stars in our sample rotate generally faster than our 1.5 d limit, while the oldest ones tend to have very low amplitudes of spectral activity. There are, however, a few remarkable exceptions to the intermediate ages, such as two relatively old stars in the Galactic thick disk (V1352 Ori, LP 734–42) and a dozen young star candidates. Among the last ones, there are bona fide members in young stellar kinematic groups, such as YZ CMi in β Pictoris (Alonso-Floriano et al. 2015a) and LP 731–76 in TW Hya (Gagné et al. 2015), and M dwarfs in the galactic young disk, not ascribed to any group, but with a plethora of youth indicators, such as 1RXS J114728.8+664405, TYC 3529–1437–1, and EV Lac, just to cite a few (Shkolnik et al. 2009; Cortés-Contreras et al. 2024). We were able to identify between 7 and 16 clusters of activity indicators exactly at the periods reported in the literature for four of the five young stars above. The fifth young star, namely LP 731–76, has neither a reported period nor a period identified by us, despite its higher X-ray, near-UV, and Hα emission and stronger magnetic field than field stars of the same spectral type. The lack of any rotation period reported may be due to a homogeneous distribution of heterogeneities on the surface of the star.

4.1.4. Predictive power of the activity indicators

Our cluster analysis can inform on the ability of each indicator to trace rotation. To do so, we investigated the types of activity indicators that formed the clusters corresponding to the stellar rotation signal. For a general overview, we show in Fig. 6 how frequently each indicator belongs to the cluster that matches the literature period either directly or is in an alias or harmonic relation, respectively. The plot gives a good indication of the predictive power of the individual indicators regarding the stellar rotation period. There is however a caveat. Results may differ if indicators are examined independently of each other (e.g. Schöfer et al. 2019, 2022; Lafarga et al. 2021). The reason is that in our case the existence of a cluster is a requirement to be counted. This means that an indicator may individually show a signal at the rotation period but not appear in the graph because there are no other indicators showing the same signal.

The CCF-FWHM from the VIS channel of CARMENES overall performs best and occurs in 35 of the 52 detected clusters whose period matches the literature period in some form. RV is, as expected among the best performing indicators, especially sensitive for active stars. Similar overall performance is shown by Ca II IRT and the Hα indices, which however mostly

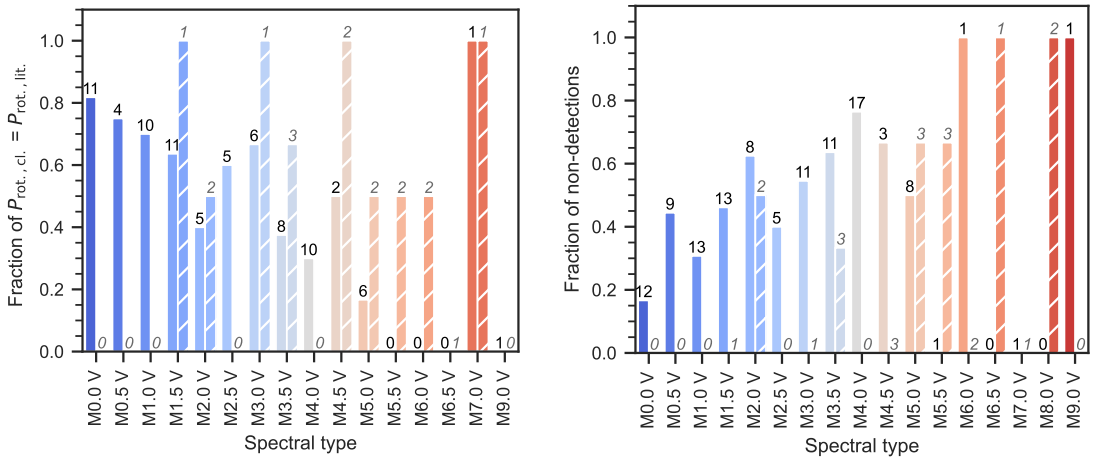

Fig. 5. Recovery rate and fraction of non-detections of stellar rotation period as a function of stellar spectral type. *Left*: fraction of stars for which the literature periods were recovered (either directly or in a harmonic or alias relation). *Right*: fraction of stars that show no significant clusters (including stars without a literature rotation period). In the plots we distinguish between inactive and active (pEW(Hα) < −0.5 Å) stars by using solid and hatched bars, respectively. In the left panel, the number on top of each bar denotes the number of stars with a known rotation period for each category. In the right panel, it yields the overall number of stars in the selected sample. For better readability, we chose normal black font for the inactive sample and italic grey font for the active sample.

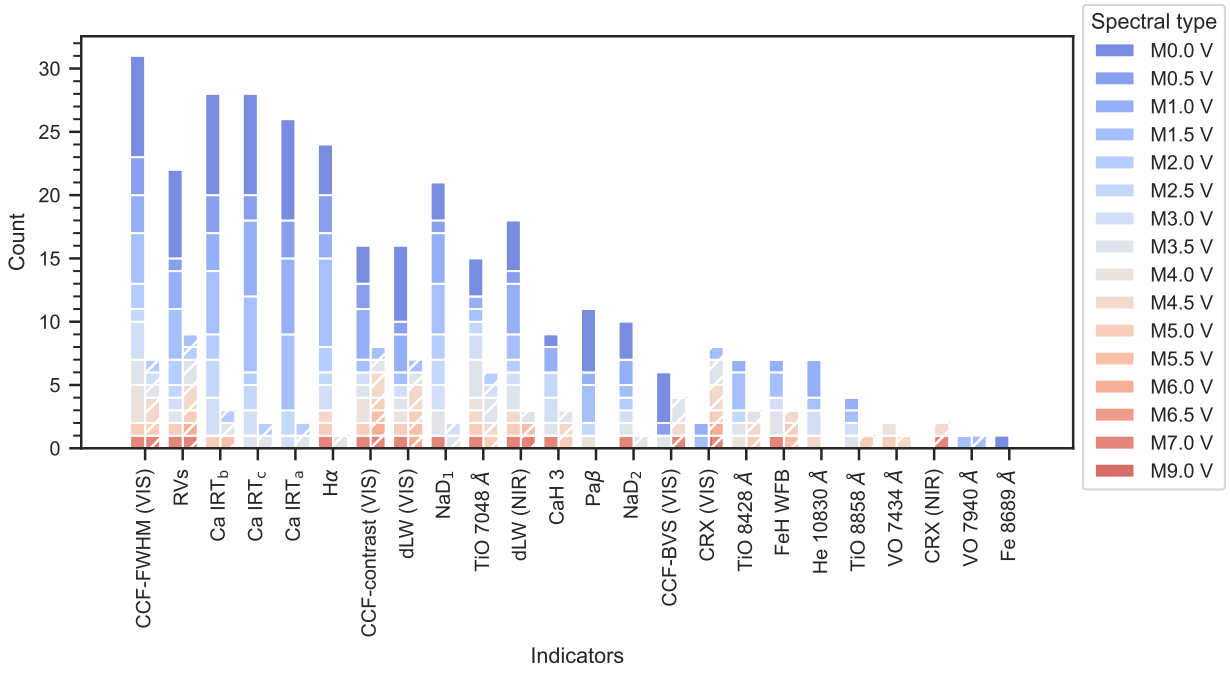

Fig. 6. Histogram showing how often individual indicators were part of clusters that matched stellar rotation periods from the literature (either directly or in a harmonic or alias relation). The different colours show the total counts in each bar, differentiated by stellar spectral type. We distinguish between inactive and active (pEW(Hα) < −0.5 Å) stars by using solid and hatched bars respectively.

appear for Hα-inactive stars. Further, while the CCF-FWHM, RVs, and Hα perform well for all spectral types, a signal of the stellar rotation period in Ca II IRT is only detected for M dwarfs of early spectral types. The latter holds also for the Na I doublet, where, interestingly, the Na D_1 line is performing considerably better than the Na D_2 and has twice the number of detections.

The diagnostic parameters of the dLW of both VIS and NIR channels, VIS-CCF-contrast, VIS-CRX, and CCF-BIS are independent of the spectral type just like the CCF-FWHM. However, they have a lower predictive power regarding the stellar rotation. Interestingly, the dLW from both channels perform similarly well, and in general better than the CRX of both channels.

Of the photospheric band indices, TiO λ7048 Å is particularly remarkable. Excluding diagnostic indicators, TiO λ7048 Å is the most sensitive for both active and non-active stars. Additionally, in contrast to most of the other indicators, it seems to be overall also sensitive for mid-M dwarfs, where our recovery rate in general was pretty low. The CRX and Fe λ8689 Å indicators both trace rotation better for the active than the inactive stars. It is noticeable that the indicator He I D_3 was never found in the rotation period clusters and, therefore, does not appear in Fig. 6. The possible reason for this is that the He I D_3 line only shows variability in very active stars, of which there are only a few in our sample.

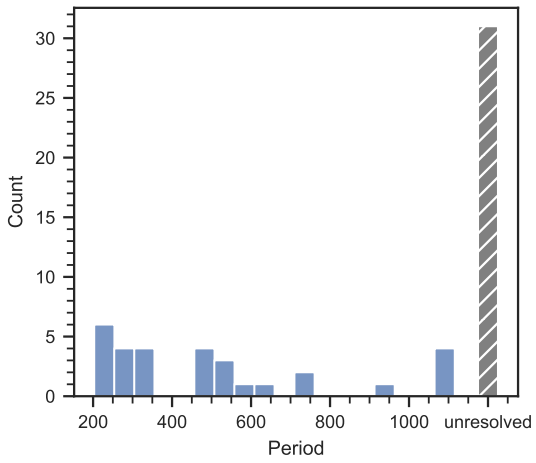

Fig. 7. Period distribution of the long-term signals ($P > 200$ d) detected by the automated clustering algorithm.

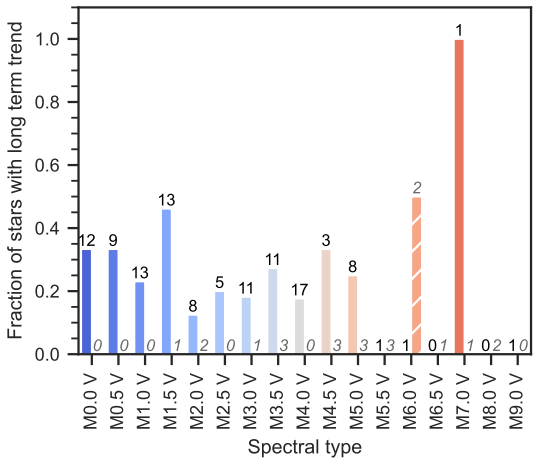

Fig. 8. Same as Fig. 5, but for fraction of stars that show long-term signals in the clustering algorithm.

An interesting application of the clustering algorithm is that it also allows for an investigation of the relations between the indicators, which we present in Appendix B. The main result is that indicators of the same kind are likely to appear together in clusters, since they are often affected by activity in the same way and, therefore, show the same signals. This partly explains, for example, why the CCF indicators and Ca II IRT are particularly frequent in the clusters, as they can form clusters by themselves. It also highlights a strength of the clustering analysis. A good indication of its genuine nature is when a cluster contains several data points from indicators of the same type, which can be easily traced. However, we note than one cannot completely discard similar indicators to be similarly affected by the same biases.

4.2. Detecting long-term cycles

In addition to determining the stellar rotation period, we used the automatic clustering algorithm of our sample to look for long-term activity cycles in the data. We considered periodicities above 200 d to be cycle candidates. We found 40 stars (29 %) that have clusters with periods greater than 200 d that are unrelated to the periods that we determined as the stellar rotation periods (see Table C.2 for an overview). The majority of these identifications (31) are signals with periods corresponding to the timespan of the observations, which indicates unresolved long-term trends that appear as a plateau for longer periods in the periodograms (see Fig. 7). The rest seem to be divided into roughly three groups with periods around 300 d, 450–750 d, and 950–1150 d.

The strong concentration around the multiples of a year is suspicious and suggests that some signals might be false positives. Since a detailed investigation of all our detections as, for example, Fuhrmeister et al. (2023), would be beyond the scope of this work, we therefore concentrated our further analysis on the unexplained signals. They usually have longer baselines and are more consistent with the measurements of activity cycles from photometry and the $R'_{\rm HK}$ index (Suárez Mascareño et al. 2016; Díez Alonso et al. 2019; Fuhrmeister et al. 2023).

As in Sect. 4.1, we looked for a possible correlation between detected clusters and stellar spectral type (see Fig. 8). Because the overall number of detections is low, any interpretation has to be taken with caution, but in general a lower fraction of the mid-type M dwarfs seems to show long-term trends. The majority of the detections come from inactive stars. There are only two active stars with signals, both late type stars. In Fig. 9 we show the breakdown of the indicators that are present in the clusters of the long-term trends. Overall, the distribution exhibits some differences in comparison to Fig. 6. For example, there seems to be no bias of the indicators regarding spectral types. Further, in contrast to the stellar rotation periods, the CCF-FWHM is much less frequent in clusters of long-term signals. Also, the CCF-contrast and Na D_1 perform much better for the longer periods than for the shorter rotation periods.

4.3. Non activity-related signals

4.3.1. Clustering at the lunar cycle

The alias pair of 27.4 d and 29.4 d occurring in the clustering diagram of Teegarden's star led us to look for similar signals in our entire sample and investigate the possible contamination of our spectra by lunar stray light. We found five stars with clusters appearing at 27–30 d. However, all of these could either be explained as likely harmonics of a known stellar rotation period as in the case of Teegarden's star or were associated with inactive stars that did not show any activity related signals in our analysis and have unconfirmed rotation periods according to Shan et al. (2024). If, indeed, these inactive stars do not show variability-related signals in the periodogram, this would mean that these signals at 27–30 d could actually be caused by the sampling of the data. This is because RVs are often taken on bright nights, which imprints the lunar cycle into the window function of the sampling. We therefore assumed that contamination by the lunar spectrum has no significant influence on our activity indicators.

4.3.2. Clustering at the harmonics of one year

Signals around the period of one year and its integer fractions occur persistently in the clustering analysis, even when using the pre-whitening method for the signal search. It is present for 120 of the 136 targets in the sample and covers periods ranging from a full year to a sixth or a seventh of a year (see Fig. 10). Though those signals also often appear in periodograms of activity indicators in the literature (e.g. Kossakowski et al. 2023; Standing et al. 2023; Sartori et al. 2023; Lee et al. 2023), they are seldom specifically addressed. They are probably not independent harmonic signals, as is often assumed, and could be concluded from the fact that they occur despite our pre-whitening of the

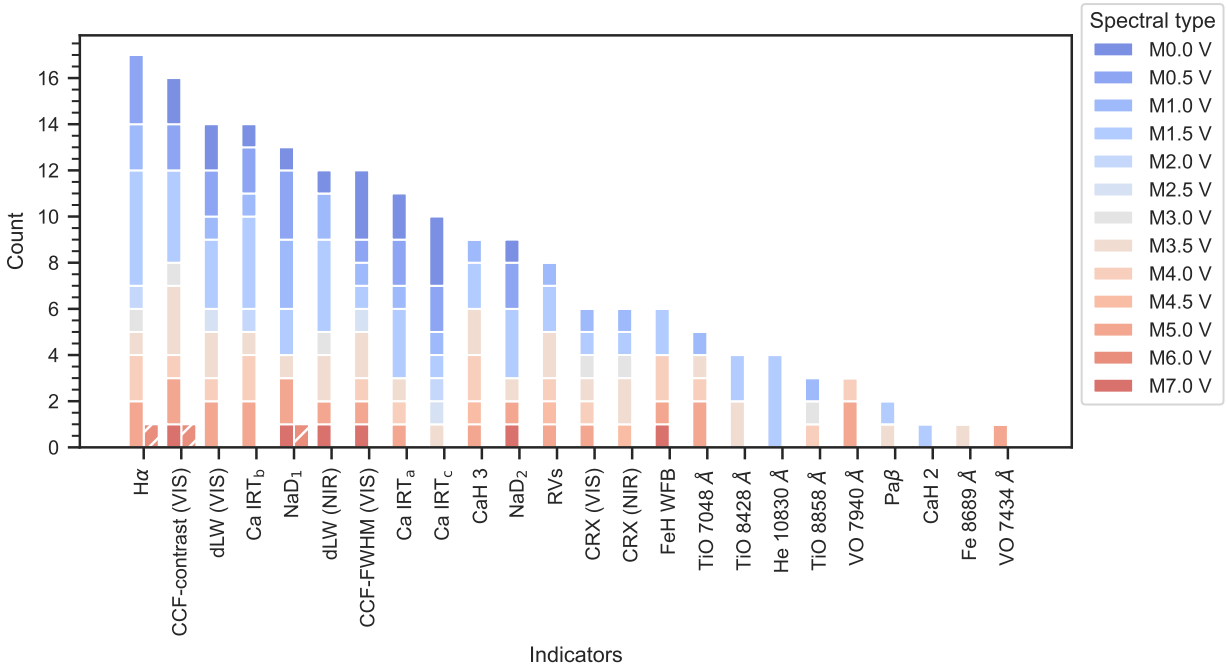

Fig. 9. Histogram of the activity indicators that appear in clusters of long-term signals. The different colours show the total counts in each bar, differentiated by stellar spectral type. We distinguish between inactive and active (pEW(Hα) < −0.5 Å) stars by using solid and hatched bars, respectively.

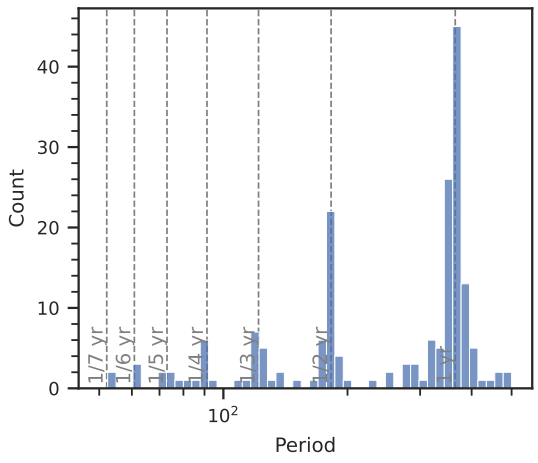

Fig. 10. Period distribution of signals occurring around 1 year and its integer fractions.

periodograms. Instead, we propose that they are aliases of a spurious signal of about one year affecting the data.

The coincidence seen among the view of harmonics and aliases is explained by the fact that besides the usually dominant sampling frequency of one day in the window function of the data, there is also often a yearly sampling frequency apparent (since most stars are only observable seasonally), which can produce the observed periods[2]. In principle, the distinguishing feature is that in the case of aliasing, the occurring signals in the clustering analysis depend on the actual dominant frequencies in the window function of the data, and we do not expect an indicator to show up in multiple clusters of the series if we use the pre-whitening method as we do here. In contrast, in the case of harmonics, we expect a fixed ratio between the occurring signals and an indicator can show up in multiple clusters as they are independent of each other.

The vast majority of the clusters in the sample that are related to one year and its integer fractions (hereafter, spurious clusters) are consistent with both explanations. The reason is that in many cases the sampling frequency is very close to one year, so that aliases and harmonics cannot be distinguished within the uncertainties (i.e. the scatter within the cluster or the resolution of the GLS). In addition, for most of the targets, we did not find more than two spurious clusters, which inhibits a meaningful analysis of the repeated occurrence of indicators. We therefore limited our analysis to the few stars whose sampling deviates significantly from the period of 1 year or that have a particularly large number of clusters related to 1 year.

In doing so, we found evidence for the presence of both aliasing and harmonics. For example, HD 147379 (Reiners et al. 2018a) has an apparent sampling frequency in the window function of the data of $\sim 1/430\,d^{-1}$ and shows an alias pair at 372 d and 203 d that is inconsistent with being harmonics. On the contrary, BD+11 2576 ($f_s = 1/379\,\mathrm{d}^{-1}$) shows a regular harmonic series of 366 d, 179 d, 121 d, 91 d and 74 d, where the indicators CaH 3, He I λ10 830 Å and TiO λ8858 Å each appear three times in different clusters. Most importantly, however, we also found a relationship between the occurrence of multiple spurious clusters and the presence of long-term cycles in the clustering analysis. Our resulting hypothesis is that the same indicators appearing in different clusters may not be symptomatic of harmonics, but the result of a non-ideal model in the pre-whitening in the signal search for the stars with long-term trends.

In the case of aliasing, the cause of the underlying signal is unlikely to be a purely sampling effect due to the frequencies in the window function. Reasons for this are, for example, that the clusters around a year also occur in combination with

[2] Aliasing occurs at $f_a = f_u \pm m f_s$ (where f_a is the alias frequency, f_u the underlying signal, f_s the sampling frequency and m is an integer value). For an underlying signal with a period of one year and a yearly sampling, it follows for positive m: $f_a = (m+1)/365$, which corresponds to the harmonics of 1 year in period space.

very strong signals of stellar activity, contrary to the fact that the sampling periods usually only appear for very homogenous data (Dawson & Fabrycky 2010). Furthermore, while we would expect a positive correlation between the occurring cluster periods and the sampling frequencies if they were the same, we actually determined a slightly negative correlation (Pearson correlation coefficient of $r = -0.19$).

5. Discussion

5.1. Clustering as a method to determine stellar rotation periods

Our comparison of the periods obtained from activity indicator clustering with the rotation periods reported in the literature showed that our method can be an effective tool for the determination of stellar rotation periods. We have also shown that pre-whitening the data prior to analysis leads to fewer false-positive detections. However, because the automatic search often finds aliases or harmonics of the literature rotation period, complementary photometric observations and a detailed manual analysis of the occurring cluster periods, like we presented for Teegarden's star, should be used to confirm the results. False negative detections (rotation periods identified by one method but not the other) can occur when the rotation period overlaps with an alias frequency (in the case of the naive method) or loss of samples (in the case of the pre-whitening method). Therefore, comparing the naive and pre-whitening results can help detect these false negatives.

In this work, we focussed on a homogeneous analysis of the spectral activity indicators. It would be interesting to extend the clustering analysis to photometry data. Note that the photometry must have comparable temporal resolution as that of the spectral activity indicators, since the method uses a universal distance parameter for all data points in the clustering. In our work, we did not use photometry because it is only available for a sub-sample of our data set and has a wide scatter in temporal resolution (Díez Alonso et al. 2019; Shan et al. 2024).

The current implementation of our method to search for stellar rotation periods has some limitations. Since we restrict the analysis to periods longer than 1.5 days, our method is unsuitable for the analysis of fast rotators. Furthermore, the exclusion of signals around one year and its harmonics means that it would also miss any true signals occurring at these periods. Therefore, for stars exhibiting high activity (i.e. likely fast rotators) or yield negative detections, it is recommended to perform manual inspection and signal searches on an unrestricted frequency range. In the case of fast rotators, dense photometric monitoring remains the most efficient and effective way to determine rotation periods, especially in the era of TESS.

Furthermore, the performance of our method is sensitive to the stability, longevity, and intensity contrast of active regions. Since active regions can be complex and have finite lifetimes, observations over long timespans might trace different active regions. This complexity and time-evolution can result in low significance and non-coherent periodicities in the activity indicators, which in turn can strongly affect the detection of a clear periodicity in the periodograms, especially over long timescales. There is no easy solution to this problem, but one possible mitigation strategy could be to work with selected sub-sets of data exhibiting a roughly constant activity level, if the quantity and time coverage of data permits doing so with minimal loss to signal significance (see e.g. Schöfer et al. 2022).

5.2. Influence of the spectral type and the global activity level

Using the information from the clustering analysis, we analysed the relations between the different activity indicators and the stellar properties. We were able to reproduce a number of results from previous studies of the activity indicators.

We showed that the number of stars with clusters related to the photometric stellar rotation period is highest for early-type M stars, regardless of the Hα activity level. There is a notable lower sensitivity of the chromospheric indicators with respect to active stars compared to the diagnostic indicators, which is in agreement with the previous work of Lafarga et al. (2021) and Schöfer et al. (2022). On the contrary, the dLW and CCF-contrast perform especially well for Hα-active stars.

We found a lower detection rate of rotation periods for stars with rotation periods longer than 100 d (e.g. Lafarga et al. 2021). Besides the fact that this relation of activity and rotation periods is well known in the literature (e.g. Astudillo-Defru et al. 2017a; Newton et al. 2017), we note that also our methodology has an impact here. For the same amplitude of the signals, the phase coverage is always worse for longer rotation periods than for shorter periods given a data set with the same sampling and timespan (see e.g. Jeffers et al. 2022 for the impact of different sampling on the periodicities detected for the mid-M dwarf EV Lac). This dependency directly affects the power of the signals in the periodograms following the $\hat{\chi}^2_0$ in the denominator of Eq. (59) in VanderPlas (2018). For a quantitative analysis, a correction for the completeness of the detected signals, as it is for example usually done for retrieving occurrence rates of RV detected stars (e.g. Sabotta et al. 2021), would therefore be necessary.

5.3. Dearth of periodicities of mid-M spectral types

In this work we found a previously unreported decrease in the appearance of periodic signals related to the stellar rotation period for stars with mid-M spectral types, corresponding to the transition from partially to fully convective stars between M3.5 V to M4.5 V. The reconstruction of the large-scale magnetic field geometry using the technique of Zeeman-Doppler imaging shows that mid-M dwarfs typically have magnetic fields that are stronger and more stable than the weaker and more complex fields of early-M dwarfs, while stars with late M spectral types can have either strong and stable or weak and complex fields (Morin et al. 2008, 2010). The detailed investigation of the stellar activity of the cornerstone mid-M dwarf EV Lac by Jeffers et al. (2022), using low-resolution Doppler imaging techniques applied to CARMENES spectra over a time span of a few years, is consistent with these results is. We showed that EV Lac has a dominant large and stable activity feature, but that there is also evidence of very rapid evolution of small stellar activity features visible in the comparison of several sectors of data from the Transiting Exoplanet Survey Satellite (TESS).

In support of the presence of a component of rapid evolution are the results from Yang et al. (2023), who analysed TESS data spanning just over two years. They determined the flaring rates of more than 13 000 stars with spectral types spanning late-F to late-M. They reported that mid-M dwarfs have the highest flaring rates of their stellar sample. A possible explanation for the dearth of periodicities for mid-M dwarfs is the presence of these small-scale activity features that are below the resolution of Zeeman-Doppler imaging but are sufficiently irregular to impact the periodicities of the individual activity lines. The changes in the geometry of the surface magnetic fields underlying the flares,

caused by the transition between dynamo modes, could also be the cause (e.g. Reiners & Basri 2009; Morin et al. 2008, 2010; Kitchatinov et al. 2014; Yadav et al. 2015).

Another point to consider is the sampling rate of the observations. As an extension of the investigation of EV Lac, Jeffers et al. (2022) reported that small sub-sets of data that span not more than a few stellar rotation periods showed a remarkably high detection rate of the rotation period in the stellar activity indices. The method that we have developed in this work also has a great potential as a diagnostic of the complexity of the stellar activity features, and particularly for data sets where the rotation period of the star is densely sampled. The rapid evolution of the stellar activity indices could indicate that there is a high temporal evolution of the small scale activity features, and in the future we will investigate this further.

5.4. The predictive power of the indicators to trace rotation

How often each indicator is found in activity-related clusters also allowed us to make statements about their predictive power. The overall best performance regarding the stellar rotation period are the CCF-FWHM and the Ca II IRT. It is also notable that indicators of the same type, such as the three lines of the Ca II IRT, often show the same signals, which favours the detection of a cluster. We found that the Ca II IRT is only sensitive for inactive stars with earlier spectral types, as previously reported by Lafarga et al. (2021). The TiO λ7048 Å indicator performs best among the photospheric indicators, both for Hα-active and -inactive stars, and is particularly sensitive to the intermediate-type M dwarfs. This is in agreement with the results of Schöfer et al. (2022), who showed that TiO λ7048 Å can exhibit a rotational signal over the entire range from Hα-inactive and slowly rotating to very active and rapidly rotating stars. The fact that they are particularly sensitive to the mid-M dwarfs, in contrast to the chromospheric indicators, can be explained by a combination of two effects. First, the indicators are less sensitive to earlier spectral types because the TiO bands are generally weaker at higher temperatures. Secondly, as shown, the number of activity signals generally decreases for later spectral types, so that the optimum is reached for middle spectral types.

The equal predictive power of the VIS and NIR dLW regarding the stellar rotation period might seem contradictory since the amplitude of activity induced signals in the RV in general decreases with increasing wavelength because of the lower contrast between the spots and the stellar surface (e.g. Desort et al. 2007; Reiners et al. 2010; Anglada-Escudé et al. 2013). By design, the dLW is however specifically sensitive to line-broadening due to the Zeemann effect, which can be particularly strong at NIR wavelength (e.g. Donati & Landstreet 2009; Reiners et al. 2013, 2022). The NIR dLW indicator could therefore be a particularly good tracer for changes in the stellar magnetic activity.

Interestingly, the two Na I doublet lines show a huge difference in their predictive power, the Na D_1 line being much more efficient than Na D_2 for stars earlier than M4.0 V. The two resonant lines show a complicated behaviour, since they consist of a strong photospheric absorption component, which gets increasingly shallower for later spectral types, and a chromospheric emission core, which is not present in the least active stars. Moreover, both lines may be affected by strong airglow (Osterbrock & Martel 1992; Slanger et al. 2003). While the absorption troughs show a similar intensity, which reflects in the indices exhibiting about the same values, the weak emission cores and airglow are about a factor of two stronger in the Na D_2 line, following the $\log gf$ ratio obtained from the VALD database (Ryabchikova et al. 2015). This effect leads to the situation that in many stars an emission core can be identified in the Na D_2 line but not in the Na D_1 line. We therefore conclude that photospheric variations seem to cause the variation in the Na D_1 line, while the interplay of photospheric and chromospheric variations leads to a veiling of the periodic signatures in the Na D_2 line. This complicated behaviour deserves further attention, which is beyond the scope of this study. In previous CARMENES studies, the sum of both lines was typically analysed, which blurred out this effect. A treatment of an average of both lines indices is also usually used in the sparse literature on activity seen in the Na I doublet (e.g. Gomes da Silva et al. 2011). From our findings, a separate treatment of the two lines is advisable at least for early M dwarfs, making use of the higher sensitivity of the Na D_1 line in these stars.

Activity indicators appearing in the clusters of long-term signals showed some differences to that of the stellar rotation periods. In addition to the generally smaller sample size, the sensitivity of the activity indicators to the long-term stability of the CARMENES instrument plays a role here. For instance, it is reasonable that the CCF-contrast performs best because it remains more stable over long periods of time than the CCF-FWHM, which is much more sensitive to changes in the instrument's line spread function caused by, for example, seasonal temperature changes during the year. Further, long-term signals activity indicators based on well-defined spectral lines such as Hα have an advantage over band indices, such as the TiO indicators, which cover multiple lines that may not behave in an entirely identical manner and thus introduce intrinsic scatter.

5.5. Clustering at spurious periods

While contamination from the lunar spectrum does not have a significant impact on our activity indicators, the signals around one year and its integer fractions are ubiquitous. Our hypothesis is that these signals are not likely to be independent harmonic signals, but instead aliases of only one underlying signal affecting the activity indicators. While there is some scatter in the actual period due to the uncertainties in the periodograms, the root of the signal seems to be closely related to a period of one year and does not depend on the sampling of the data. We observed that a pure sinusoid is not sufficient to model the variations in all cases, suggesting that the variability in the activity indicators could be caused by a process that is only quasi-periodic. Possible explanations include variations of the line spread function caused by recurring disturbances on the instrument, such as small annual temperature or pressure changes in the instrument room (Bauer et al. 2020). External influences such as changes in the ambient temperature and, therefore, the chemistry of the atmosphere can also lead to a varying contamination of the spectra. For example, we saw similar signals with a period of about one year for the RVs of CARMENES survey stars, which are caused by contamination by telluric lines (Nagel et al. 2023). In the case of an atmospherical origin, we would however expect these signals to have some dependency on the stellar spectral type that we did not observe. Further, we did not see a clear correlation between the signals in the telluric contaminated RVs and the activity indicators.

Based on these assumptions, pre-whitening of the periodograms is an important and appropriate tool to uncover the actual activity signals in the data. However, because the changes imprinted onto the spectra seem to be only of a quasi-periodic nature, a simple sinusoidal model can still lead to residual signals

at the aliases of one year, which needs to be considered during the analysis of the clustering results. Our approach of removing all signals close to one year and its integer fractions from the data before applying the clustering algorithm is a simple way to reduce those residuals.

5.6. Occurrence of long-term cycles

The accumulation of the long-term activity cycles around multiples of one year that we found should be a warning sign regarding their veracity. A plausible explanation is that some of the signals are related to spurious signals. The clustering analysis as a method for detecting long-period signals should therefore not be used on its own, but only in combination with other complementary measurements.

The unexplained long-term cycles are preferentially detected in inactive stars. Presumably, this is an observational bias, since active stars are noisier, which complicates the detection. Apart from this, as described in the previous section for the longest rotation periods, our method of searching for signals with the GLS periodogram is biased towards shorter periods. As a result, a correction for the completeness of the detected signals would be mandatory in quantitative analysis.

6. Conclusion

We present a novel approach to detecting stellar rotation periods and other stellar activity signals in the periodograms of the time series of stellar activity spectral indicators by using a machine learning clustering algorithm. This approach shows promise in identifying spectroscopic modulations related to stellar rotation and can be used to complement rotation period measurements from stellar photometric variability. Analysing the identified clusters makes it possible to combine the information content in many activity indicators simultaneously and also to include signals with higher FAPs in the analysis. It is a way to organize and interpret the multitude of signals occurring in various spectroscopic indicators. Using this method, we demonstrate the successful recovery of 56 rotation periods consistent with those in the literature, and report three new periods.

The benefit of combining several indicators is illustrated by our analysis of the relationships of the indicators to each other, as well as to the stellar properties. The individual indicators have different sensitivities to different aspects of stellar activity. A large survey with extensive spectroscopic and temporal coverage, such as CARMENES, provides an excellent opportunity to explore the imprints of stellar activity phenomena on a variety of spectroscopic indicators. The cluster analysis presented here is a powerful tool for investigating relationships between the indicators and stellar activity. This approach will be potentially useful for uncovering other activity-sensitive lines, as well as laying the groundwork for understanding their physical origins.

Acknowledgements. The authors thank the anonymous referee for their helpful comments that improved the quality of the manuscript. This publication was based on observations collected under the CARMENES Legacy+ project. CARMENES is an instrument at the Centro Astronómico Hispano en Andalucía (CAHA) at Calar Alto (Almería, Spain), operated jointly by the Junta de Andalucía and the Instituto de Astrofísica de Andalucía (CSIC). The authors wish to express their sincere thanks to all members of the Calar Alto staff for their expert support of the instrument and telescope operation. CARMENES was funded by the Max-Planck-Gesellschaft (MPG), the Consejo Superior de Investigaciones Científicas (CSIC), the Ministerio de Economía y Competitividad (MINECO) and the European Regional Development Fund (ERDF) through projects FICTS-2011-02, ICTS-2017-07-CAHA-4, and CAHA16-CE-3978, and the members of the CARMENES Consortium (Max-Planck-Institut für Astronomie, Instituto de Astrofísica de Andalucía, Landessternwarte Königstuhl, Institut de Ciències de l'Espai, Institut für Astrophysik Göttingen, Universidad Complutense de Madrid, Thüringer Landessternwarte Tautenburg, Instituto de Astrofísica de Canarias, Hamburger Sternwarte, Centro de Astrobiología and Centro Astronómico Hispano-Alemán), with additional contributions by the MINECO, the Deutsche Forschungsgemeinschaft through the Major Research Instrumentation Programme and Research Unit FOR2544 "Blue Planets around Red Stars", the Klaus Tschira Stiftung, the states of Baden-Württemberg and Niedersachsen, and by the Junta de Andalucía. We acknowledge financial support from a UKRI Future Leader Fellowship grant number MR/S035214/1, the UKRI grant EP/X027562/1, the ERDF "A way of making Europe" through project PID2019-109522GB-C5[1,2,3,4], the DFG priority program SPP 1992 "Exploring the Diversity of Extrasolar Planets" (JE 701/5-1), and the Research Council of Norway through the Centres of Excellence funding scheme, project number 332523 (PHAB). The analysis of this work has made use of a wide variety of public available software packages that are not referenced in the manuscript: `scipy` (Virtanen et al. 2020), `NumPy` (Harris et al. 2020), `matplotlib` (Hunter 2007), `tqdm` (da Costa-Luis 2019), `pandas` (The pandas development team 2020; Wes McKinney 2010), `seaborn` (Waskom 2021).

References

Alonso-Floriano, F. J., Caballero, J. A., Cortés-Contreras, M., Solano, E., & Montes, D. 2015a, A&A, 583, A85
Alonso-Floriano, F. J., Morales, J. C., Caballero, J. A., et al. 2015b, A&A, 577, A128
Amado, P. J., Bauer, F. F., Rodríguez López, C., et al. 2021, A&A, 650, A188
Anglada-Escudé, G., Butler, R. P., Reiners, A., et al. 2013, Astron. Nachr., 334, 184
Astropy Collaboration (Price-Whelan, A. M., et al.) 2018, AJ, 156, 123
Astudillo-Defru, N., Delfosse, X., Bonfils, X., et al. 2017a, A&A, 600, A13
Astudillo-Defru, N., Forveille, T., Bonfils, X., et al. 2017b, A&A, 602, A88
Baliunas, S. L., Donahue, R. A., Soon, W. H., et al. 1995, ApJ, 438, 269
Baluev, R. V. 2008, MNRAS, 385, 1279
Barnes, J. R., Jeffers, S. V., & Jones, H. R. A. 2011, MNRAS, 412, 1599
Barnes, J. R., Jeffers, S. V., Haswell, C. A., et al. 2024, MNRAS, 534, 1257
Baroch, D., Morales, J. C., Ribas, I., et al. 2018, A&A, 619, A32
Baroch, D., Morales, J. C., Ribas, I., et al. 2021, A&A, 653, A49
Bauer, F. F., Zechmeister, M., Kaminski, A., et al. 2020, A&A, 640, A50
Berdyugina, S. V., & Solanki, S. K. 2002, A&A, 385, 701
Boisse, I., Moutou, C., Vidal-Madjar, A., et al. 2009, A&A, 495, 959
Boisse, I., Bouchy, F., Hébrard, G., et al. 2011, A&A, 528, A4
Brandenburg, A., Mathur, S., & Metcalfe, T. S. 2017, ApJ, 845, 79
Caballero, J. A., & Dinis, L. 2008, Astron. Nachr., 329, 801
Castro-Ginard, A., Jordi, C., Luri, X., et al. 2018, A&A, 618, A59
Cortés-Contreras, M., Caballero, J. A., Montes, D., et al. 2024, A&A, 692, A206
da Costa-Luis, C. 2019, J. Open Source Softw., 4, 1277
Dawson, R. I., & Fabrycky, D. C. 2010, ApJ, 722, 937
Desidera, S., Gratton, R. G., Endl, M., et al. 2004, A&A, 420, L27
Desort, M., Lagrange, A. M., Galland, F., Udry, S., & Mayor, M. 2007, A&A, 473, 983
Díaz, R. F., Delfosse, X., Hobson, M. J., et al. 2019, A&A, 625, A17
Díez Alonso, E., Caballero, J. A., Montes, D., et al. 2019, A&A, 621, A126
Donati, J. F., & Landstreet, J. D. 2009, ARA&A, 47, 333
Donati, J. F., Lehmann, L. T., Cristofari, P. I., et al. 2023, MNRAS, 525, 2015
Dreizler, S., Luque, R., Ribas, I., et al. 2024, A&A, 684, A117
Ester, M., Kriegel, H.-P., Sander, J., & Xu, X. 1996, in Proceedings of the Second International Conference on Knowledge Discovery and Data Mining, KDD'96 (AAAI Press), 226
Figueira, P., Marmier, M., Bonfils, X., et al. 2010, A&A, 513, L8
Fouqué, P., Martioli, E., Donati, J. F., et al. 2023, A&A, 672, A52
Fuhrmeister, B., Czesla, S., Schmitt, J. H. M. M., et al. 2019, A&A, 623, A24
Fuhrmeister, B., Czesla, S., Perdelwitz, V., et al. 2023, A&A, 670, A71
Fuhrmeister, B., Schmitt, J. H. M. M., Reiners, A., et al. 2024, A&A, 691, A208
Gagné, J., Lafrenière, D., Doyon, R., Malo, L., & Artigau, É. 2015, ApJ, 798, 73
Gomes da Silva, J., Santos, N. C., Bonfils, X., et al. 2011, A&A, 534, A30
Gomes da Silva, J., Santos, N. C., Bonfils, X., et al. 2012, A&A, 541, A9
Harris, C. R., Millman, K. J., van der Walt, S. J., et al. 2020, Nature, 585, 357
Hatzes, A. P. 2013, ApJ, 770, 133
Hatzes, A. P. 2019, The Doppler Method for the Detection of Exoplanets (Bristol, UK: IOP Publishing)
Haywood, R. D., Collier Cameron, A., Queloz, D., et al. 2014, MNRAS, 443, 2517
Houdebine, E. R., Junghans, K., Heanue, M. C., & Andrews, A. D. 2009, A&A, 503, 929
Huélamo, N., Figueira, P., Bonfils, X., et al. 2008, A&A, 489, L9
Hunt, E. L., & Reffert, S. 2021, A&A, 646, A104

Hunter, J. D. 2007, Comput. Sci. Eng., 9, 90
Jeffers, S. V., Schöfer, P., Lamert, A., et al. 2018, A&A, 614, A76
Jeffers, S. V., Barnes, J. R., Schöfer, P., et al. 2022, A&A, 663, A27
Jeffers, S. V., Kiefer, R., & Metcalfe, T. S. 2023, Space Sci. Rev., 219, 54
Jeffers, S. V., Barnes, J. R., Schöfer, P., et al. 2025, A&A, 696, A27
Kemmer, J., Dreizler, S., Kossakowski, D., et al. 2022, A&A, 659, A17
Kitchatinov, L. L., Moss, D., & Sokoloff, D. 2014, MNRAS, 442, L1
Kossakowski, D., Kürster, M., Henning, T., et al. 2022, A&A, 666, A143
Kossakowski, D., Kürster, M., Trifonov, T., et al. 2023, A&A, 670, A84
Lafarga, M., Ribas, I., Lovis, C., et al. 2020, A&A, 636, A36
Lafarga, M., Ribas, I., Reiners, A., et al. 2021, A&A, 652, A28
Lee, S., Notsu, Y., & Sato, B. 2023, PASJ, 75, 446
Lépine, S., Rich, R. M., & Shara, M. M. 2007, ApJ, 669, 1235
Liebing, F., Jeffers, S. V., Reiners, A., & Zechmeister, M. 2021, A&A, 654, A168
Lovis, C., Dumusque, X., Santos, N. C., et al. 2011, arXiv e-prints [arXiv:1107.5325]
Luque, R., Nowak, G., Pallé, E., et al. 2018, A&A, 620, A171
Luque, R., Fulton, B. J., Kunimoto, M., et al. 2022, A&A, 664, A199
Martínez-Arnáiz, R., Maldonado, J., Montes, D., Eiroa, C., & Montesinos, B. 2010, A&A, 520, A79
Mignon, L., Meunier, N., Delfosse, X., et al. 2023, A&A, 675, A168
Morin, J., Donati, J. F., Petit, P., et al. 2008, MNRAS, 390, 567
Morin, J., Donati, J. F., Petit, P., et al. 2010, MNRAS, 407, 2269
Nagel, E., Czesla, S., Kaminski, A., et al. 2023, A&A, 680, A73
Newton, E. R., Irwin, J., Charbonneau, D., et al. 2016, ApJ, 821, 93
Newton, E. R., Irwin, J., Charbonneau, D., et al. 2017, ApJ, 834, 85
Newton, E. R., Mondrik, N., Irwin, J., Winters, J. G., & Charbonneau, D. 2018, AJ, 156, 217
Osterbrock, D. E., & Martel, A. 1992, PASP, 104, 76
Pedregosa, F., Varoquaux, G., Gramfort, A., et al. 2011, J. Mach. Learn. Res., 12, 2825
Queloz, D., Henry, G. W., Sivan, J. P., et al. 2001, A&A, 379, 279
Quirrenbach, A., Amado, P. J., Caballero, J. A., et al. 2014, SPIE Conf. Ser., 9147, 91471F
Quirrenbach, A., Amado, P. J., Caballero, J. A., et al. 2016, SPIE Conf. Ser., 9908, 990812
Rajpaul, V., Aigrain, S., Osborne, M. A., Reece, S., & Roberts, S. 2015, MNRAS, 452, 2269
Rajpaul, V., Aigrain, S., & Roberts, S. 2016, MNRAS, 456, L6
Reiners, A., & Basri, G. 2009, A&A, 496, 787
Reiners, A., Bean, J. L., Huber, K. F., et al. 2010, ApJ, 710, 432
Reiners, A., Joshi, N., & Goldman, B. 2012, AJ, 143, 93
Reiners, A., Shulyak, D., Anglada-Escudé, G., et al. 2013, A&A, 552, A103
Reiners, A., Ribas, I., Zechmeister, M., et al. 2018a, A&A, 609, L5
Reiners, A., Zechmeister, M., Caballero, J. A., et al. 2018b, A&A, 612, A49
Reiners, A., Shulyak, D., Käpylä, P. J., et al. 2022, A&A, 662, A41
Ribas, I., Reiners, A., Zechmeister, M., et al. 2023, A&A, 670, A139
Robertson, P., Endl, M., Cochran, W. D., & Dodson-Robinson, S. E. 2013, ApJ, 764, 3
Robertson, P., Endl, M., Henry, G. W., et al. 2015, ApJ, 801, 79
Ryabchikova, T., Piskunov, N., Kurucz, R. L., et al. 2015, Phys. Scr, 90, 054005
Sabotta, S., Schlecker, M., Chaturvedi, P., et al. 2021, A&A, 653, A114
Santos, N. C., Mortier, A., Faria, J. P., et al. 2014, A&A, 566, A35
Sartori, L. F., Lovis, C., Delisle, J.-B., et al. 2023, A&A, 670, A42
Schöfer, P. 2021, PhD thesis, Georg August University of Gottingen, Germany
Schöfer, P., Jeffers, S. V., Reiners, A., et al. 2019, A&A, 623, A44
Schöfer, P., Jeffers, S. V., Reiners, A., et al. 2022, A&A, 663, A68
Shan, Y., Revilla, D., Skrzypinski, S. L., et al. 2024, A&A, 684, A9
Shkolnik, E., Liu, M. C., & Reid, I. N. 2009, ApJ, 699, 649
Slanger, T. G., Cosby, P. C., Osterbrock, D. E., Stone, R. P. S., & Misch, A. A. 2003, PASP, 115, 869
Standing, M. R., Sairam, L., Martin, D. V., et al. 2023, Nat. Astron., 7, 702
Stelzer, B., Damasso, M., Scholz, A., & Matt, S. P. 2016, MNRAS, 463, 1844
Stock, S., Kemmer, J., Reffert, S., et al. 2020a, A&A, 636, A119
Stock, S., Nagel, E., Kemmer, J., et al. 2020b, A&A, 643, A112
Suárez Mascareño, A., Rebolo, R., González Hernández, J. I., & Esposito, M. 2015, MNRAS, 452, 2745
Suárez Mascareño, A., Rebolo, R., & González Hernández, J. I. 2016, A&A, 595, A12
Suárez Mascareño, A., Rebolo, R., González Hernández, J. I., & Esposito, M. 2017, MNRAS, 468, 4772
Suárez Mascareño, A., Rebolo, R., González Hernández, J. I., et al. 2018, A&A, 612, A89
Suárez Mascareño, A., González-Álvarez, E., Zapatero Osorio, M. R., et al. 2023, A&A, 670, A5
Tal-Or, L., Zechmeister, M., Reiners, A., et al. 2018, A&A, 614, A122
Terrien, R. C., Keen, A., Oda, K., et al. 2022, ApJ, 927, L11
The pandas development team 2020, https://doi.org/10.5281/zenodo.3509134
Toledo-Padrón, B., González Hernández, J. I., Rodríguez-López, C., et al. 2019, MNRAS, 488, 5145
VanderPlas, J. T. 2018, ApJS, 236, 16
Virtanen, P., Gommers, R., Oliphant, T. E., et al. 2020, Nat. Methods, 17, 261
Waskom, M. 2021, J. Open Source Softw., 6, 3021
Watson, C. L., Henden, A. A., & Price, A. 2006, Society for Astronomical Sciences Annual Symposium, 25, 47
Wes McKinney. 2010, in Proceedings of the 9th Python in Science Conference, eds. Stéfan van der Walt, & Jarrod Millman, 56
West, A. A., Hawley, S. L., Walkowicz, L. M., et al. 2004, AJ, 128, 426
Wilson, O. C. 1968, ApJ, 153, 221
Yadav, R. K., Christensen, U. R., Morin, J., et al. 2015, ApJ, 813, L31
Yang, Z., Zhang, L., Meng, G., et al. 2023, A&A, 669, A15
Zechmeister, M., & Kürster, M. 2009, A&A, 496, 577
Zechmeister, M., Reiners, A., Amado, P. J., et al. 2018, A&A, 609, A12
Zechmeister, M., Dreizler, S., Ribas, I., et al. 2019, A&A, 627, A49

Appendix A: Activity indicators used in this work

Table A.1. List of activity indicators used in the analysis.

Chromospheric line indicators [(d)]:

Indicator	Central λ [Å]	Central $\Delta\lambda$ [(a)]	Left $\Delta\lambda$ [(b)]	Right $\Delta\lambda$ [(b)]	Examined in [(c)]	Description
Hα	6562.8	±40 km s^{-1}	−500 to −300 km s^{-1}	300 to 500 km s^{-1}	Ze18, T-O18, Fu19, Sch19, La21, Je22, Sch22, Fu23	Chromospheric lines can be characterised by their emission flux in the line core. This emission flux can be measured from the line's pseudo-equivalent width (pEW) or line index, as defined in Sch19 and Ze18, respectively, for the data used here. The pEW is the equivalent width of the line with respect to a pseudo-continuum, with the spectrum of a similar non-active star subtracted from it to remove photospheric contributions. The line index is the ratio of mean flux around the line centre to the flux in reference bandpasses on either sides of the line, regions assumed to not be affected by stellar activity. Both pEW and line index measure the 0th moment of the line (i.e. depth, area, or integrated flux). We present the different lines of the Ca II infrared triplet and the Na I doublet in different rows.
Ca IRT$_a$	8498.0	±15 km s^{-1}	±40 km s^{-1} from 8492.0 Å	±40 km s^{-1} from 8504.0 Å	"	
Ca IRT$_b$	8542.1	±15 km s^{-1}	−300 to −200 km s^{-1}	250 to 350 km s^{-1}	"	
Ca IRT$_c$	8662.1	±15 km s^{-1}	−300 to −200 km s^{-1}	200 to 300 km s^{-1}	"	
Na D$_1$	5895.9	±15 km s^{-1}	±40 km s^{-1} from 5885.0 Å	±40 km s^{-1} from 5892.9 Å	Ze18, Fu19, Sch19, Je22, Sch22	
Na D$_2$	5889.9	±15 km s^{-1}	±40 km s^{-1} from 5892.9 Å	±40 km s^{-1} from 5905.0 Å	"	
He I D$_3$	5875.6	±2.5 Å	±1.25 Å from 5871.1 Å	±1.25 Å from 5881.1 Å	Sch19, Fu20, Je22, Sch22	
He I λ10 830 Å	10830.3	±0.25 Å	±1.00 Å from 10818.0 Å	±1.00 Å from 10871.7 Å	"	
Paβ	12818.1	±0.25 Å	±1.00 Å from 12813.5 Å	±1.00 Å from 12822.5 Å	Sch19, Je22, Sch22	

Photospheric absorption band indices:

Indicator	Numerator $\Delta\lambda$ [Å]	Denominator $\Delta\lambda$ [Å]	Examined in [(c)]	Description
CaH 2	6815.1 – 6817.1	6811.1 – 6813.1	Sch21, Je22	Photospheric bands can cover multiple spectral orders and are blended with other spectral features, which challenges the measurement of their pEW or line index, as typically done with chromospheric lines. Instead, photospheric band indices can be defined as the ratio of mean fluxes in two different small ranges on either side of the band head (Sch19). Similarly to chromospheric line indicators, these indices measure the 0th moment of the band absorption lines.
CaH 3	6972.1 – 6975.1	7045.1 – 7048.1	"	
TiO λ7048 Å	7054.1 – 7058.1	7044.1 – 7048.1	Sch19, Sch22, Je22, Fu23	
TiO λ8428 Å	8433.7 – 8437.7	8428.2 – 8432.2	"	
TiO λ8858 Å	8860.1 – 8862.1	8856.6 – 8858.6	"	
VO λ7434 Å	7433.9 – 7434.9	7432.3 – 7433.3	Sch19, Sch22, Je22	
VO λ7940 Å	7939.5 – 7941.5	7933.8 – 7935.8	"	
FeH WFB	9895.3 – 9904.3	9884.3 – 9893.3	Sch21, Je22	

Diagnostic indicators:

Indicator	Examined in [(c)]	Description
chromatic index (CRX) [(e)]	Ze18, T-O18, La21, Je22, Sch22	The CRX measures wavelength-dependent changes in the RVs. It is defined as the slope between the order-wise RVs and the average logarithmic wavelength of the order (Ze18).
differential line width (dLW) [(e)]	Ze18, T-O18, La21, Je22	The dLW measures differential variations in the absorption line widths of the observed spectrum with respect to a spectral template when performing a template matching minimisation (Ze18). It traces similar variations as the CCF FWHM and measures the 2nd moment of the line profile (i.e. variance).
CCF Full width at half maximum (CCF-FWHM) [(f)]	La20, La21, Je22, Sch22	The CCF represents an average shape of the stellar absorption lines, hence, its profile can be used to trace activity effects. The FWHM and the contrast are typically derived from a Gaussian fit to the CCF. The FWHM measures changes in the average width of the absorption lines (2nd moment of the CCF). The contrast traces the 0th moment of the CCF. The BIS is the difference between the average RV of the top region of the CCF profile and the average RV of the bottom region, originally defined by Queloz et al. (2001). It traces asymmetries in the line profile, so it measures the 3rd moment of the profile (skewness).
CCF bisector inverse slope (CCF-BIS) [(f)]	"	
CCF-contrast [(f)]	"	

References. Ze18: Zechmeister et al. (2018); Sch19: Schöfer et al. (2019); Sch21: Schöfer (2021); La20: Lafarga et al. (2020); T-O18: Tal-Or et al. (2018); Fu19: Fuhrmeister et al. (2019); La21: Lafarga et al. (2021); Je22: Jeffers et al. (2022); Sch22: Schöfer et al. (2022); Fu23: Fuhrmeister et al. (2023).

Notes. [(a)]Passband $\Delta\lambda$ used to integrate the flux coming from the central line, indicated in km s^{-1} from the central line, unless otherwise specified (i.e. indicated in Å for the indicators computed following Sch19). [(b)]Left and right bandpasses $\Delta\lambda$ at either side of the central line used as continuum reference, indicated in km s^{-1} from the central line, unless otherwise specified (i.e. indicated in km s^{-1} from a different reference wavelength for the Na I doublet lines, and indicated in Å from a different reference wavelength for the indicators computed following Sch19). [(c)]Listing only works by the CARMENES consortium, where underline indicates the reference where the indicator is defined. Quote (") indicates that the references are the same as in the row above. [(d)]The indicators calculated following Zechmeister et al. (2018) are dimensionless indices, while the indicators from Sch19, Sch22 are pEWs (in Å) calculated after subtracting an inactive reference star spectrum. [(e)]Calculated for the VIS and NIR channel. [(f)]Calculated only for the VIS channel.

Appendix B: Relations between the activity indicators

An advantage of the clustering method is that it additionally allowed us to directly examine the correlations between the occurrence of the activity indicators. In Fig. B.1 we show individually the incidence with which each indicator is present together with the other indicators in the clusters matching the stellar rotation period. Mainly, the diagram reflects the general frequency of the indicators from Fig. 6. It can be observed that indicators of the same type also frequently occur together, as can be expected. This is especially true for the Ca II IRT, as well as the diagnostic indicators (CCF parameters, dLW and CRX), which presumably are so abundant because they intrinsically show the same signals and can thus form their own clusters without other indicators occurring. A correlated occurrence can be further observed for the diagnostic and chromospheric indicators in general. Regarding individual indicators, it is worth mentioning that for example the TiO band indicators as photospheric indicators are found to show the highest correlation with other heavy molecules such as CaH 3 and the FeH WFB, which is likely due to their higher abundance in stars with lower temperatures (both, physically and in the frequency in the clusters). Noteworthy are the dLW, Na D_1, TiO λ7048 Å, which show interesting relations to other indicators.

Contrary to what one might expect, the dLW shows the highest correlation with the CCF-contrast and not with the CCF-FWHM (second most abundant). Both CCF-FWHM and dLW trace the variance of the line profiles, which means they represent the second moment of the line profile. The CCF-contrast measures the depth of the profile, and therefore represents the zeroth moment. The dLW, however, also has a zeroth moment component (Zechmeister et al. 2018; Jeffers et al. 2022), while the CCF-contrast and CCF-FWHM are expected to be correlated because the equivalent width of the CCF is conserved to zeroth order, which could explain the observed correlations. Furthermore, the TiO λ8858 Å index interestingly appears more often together with the CRX than other line indicators. Not unexpectedly, the Na D_1 index occurs particularly frequently with other indicators with a strong chromospheric component, such as the Ca II IRT. Yet, it also shows a particularly strong correlation with the NIR-dLW. Both CaH 3 and FeH WFB present a notable relation to the occurrence of the TiO λ7048 Å band indicator, with the FeH WFB in particular also correlating with CaH 3, and generally occurring more frequently with the three TiO band indices.

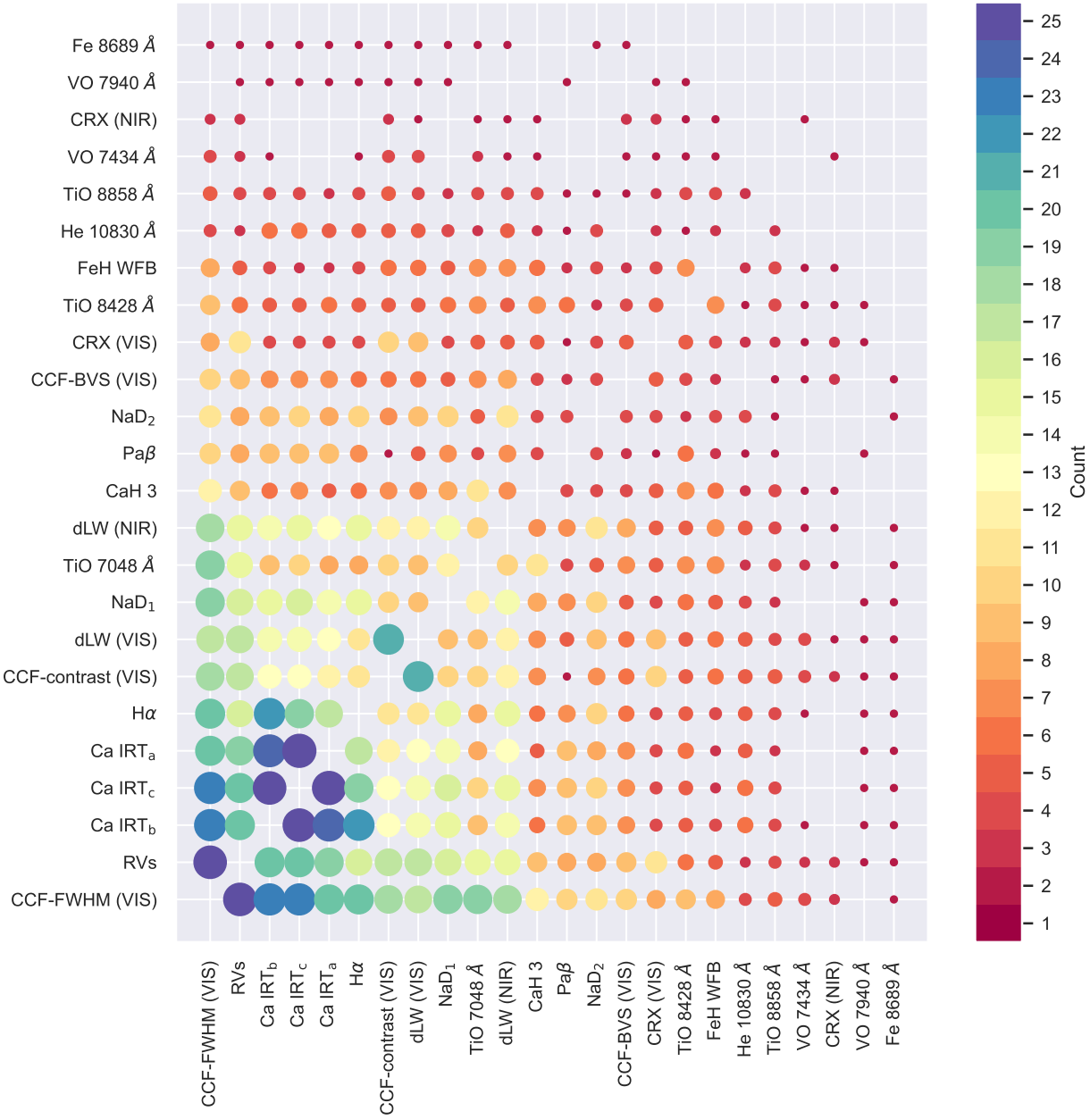

Fig. B.1. Relations between the occurrence of the indicators. The dots represent how often the individual indicators appear together in a cluster that matches the stellar rotation period (either directly or in a harmonic or alias relation). The size and colour of the dots depict the actual incidence: The bigger or bluer a dot, the more often the two indicators appear together.

Appendix C: Results tables

Table C.1. Stellar rotation periods determined from the clustering algorithm for the whole sample.

Karmn	Name	$P_{\mathrm{rot.,cl.}}$ [d]	Std. [d] [a]	GLS uncert. [d] [a]	$P_{\mathrm{rot.,lit.}}$ [d]	Ref.$_{\mathrm{lit.}}$	Reliability [b]	Match [c]	#Samples	Indicators [d]
J00051+457	BD+44 4548	…	…	…	15.37	DA19	dubious	…	…	…
J00067-075	GJ 1002	161.28	2.93	0.75	126.00	SM23	dubious	YA	6	CCF-FWHM (VIS), dLW (NIR), TiO 7048 Å, Hα, Ca IRT$_{\mathrm{c}}$, TiO 8428 Å
J00183+440	GX And	41.13	0.30	0.01	45.00	SM18	secure	D, YA	4	RVs, Ca IRT$_{\mathrm{c}}$, CCF-FWHM (VIS), Ca IRT$_{\mathrm{a}}$
J00184+440	GQ And	108.20	1.72	0.16	113.30	Don23	secure	D	7	TiO 7048 Å, CCF-FWHM (VIS), NaD$_1$, dLW (NIR), FeH WFB, NaD$_2$, Ca IRT$_{\mathrm{c}}$
J00389+306	Wolf 1056	18.31	0.05	0.01	50.20	DA19	tentative	H	3	Ca IRT$_{\mathrm{a}}$, Ca IRT$_{\mathrm{b}}$, NaD$_1$
J01025+716	Ross 318	51.98	1.56	0.07	50.52	Sh24	secure	D, YA	10	Hα, TiO 7048 Å, CCF-FWHM (VIS), dLW (VIS), CCF-contrast (VIS), Ca IRT$_{\mathrm{b}}$, Ca IRT$_{\mathrm{c}}$, CaH$_3$, TiO 8858 Å, He 10830 Å
J01026+623	BD+61 195	18.91	0.11	0.01	18.82	Sh24	secure	D, YA	8	Hα, Ca IRT$_{\mathrm{b}}$, TiO 7048 Å, Ca IRT$_{\mathrm{a}}$, Ca IRT$_{\mathrm{c}}$, CCF-FWHM (VIS), NaD$_1$, RVs
J01048-181	GJ 1028	…	…	…	143.20	New18	tentative	…	…	…
J01125-169	YZ Cet	79.82	2.09	0.11	70.10	Sh24	secure	D, YA	6	CCF-FWHM (VIS), dLW (VIS), RVs, CRX (VIS), CCF-FWHM (VIS), CCF-contrast (VIS)
J02002+130	TZ Ari	1.96	0.01	0.01	2.00	Sh24	secure	D, YA, DA	4	RVs, CCF-BVS (VIS), CRX (VIS), TiO 7048 Å
J02015+637	G 244-047	…	…	…	…	…	…	…	…	…
J02123+035	BD+02 348	…	…	…	17.11	Sh24	dubious	…	…	…
J02222+478	BD+47 612	31.13	0.08	0.01	29.50	DA19	secure	D, YA	4	Ca IRT$_{\mathrm{b}}$, Hα, Ca IRT$_{\mathrm{a}}$, CCF-FWHM (VIS)
J02362+068	BX Cet	…	…	…	…	…	…	…	…	…
J02442+255	VX Ari	…	…	…	38.70	DA19	tentative	…	…	…
J02530+168	Teegarden's Star	98.05	1.30	0.16	97.56	Laf21	tentative	D	12	CCF-contrast (VIS), CCF-FWHM (VIS), dLW (VIS), dLW (NIR), FeH WFB, NaD$_2$, CaH$_3$, TiO 7048 Å, NaD$_1$, RVs, CCF-contrast (VIS), Hα
J03133+047	CD Cet	139.71	7.09	0.54	126.20	New16	secure	D	9	TiO 7048 Å, dLW (VIS), Hα, CCF-contrast (VIS), CCF-FWHM (VIS), dLW (NIR), Ca IRT$_{\mathrm{b}}$, RVs, VO 7434 Å
J03181+382	HD 275122	…	…	…	77.20	DA19	tentative	…	…	…

References. DA19: Díez Alonso et al. (2019); SM23: Suárez Mascareño et al. (2023); SM18: Suárez Mascareño et al. (2023); Sh24: Shan et al. (2024); New18: Newton et al. (2018); Laf21: Lafarga et al. (2021); New16: Newton et al. (2016); Luq22: Luque et al. (2022); Sto20b: Stock et al. (2020b); SM17: Suárez Mascareño et al. (2017); Mor10: Morin et al. (2010); Diaz19: Díaz et al. (2019); Ste16: Stelzer et al. (2016); Luq18: Luque et al. (2018); SM15: Suárez Mascareño et al. (2015); TP19: Toledo-Padrón et al. (2019); Ama21: Amado et al. (2021); Wat06: Watson et al. (2006), Don23: Donati et al. (2023)

Notes. Rotation periods determined in this work are highlighted in bold font.

[a]Standard deviations and GLS uncertainties smaller then 0.00 d where conservatively set to 0.01 d [b]according to Shan et al. (2024) [c]YA: yearly alias match; DA: daily alias match; H: harmonic match; D: direct match [d]sorted by minimum FAP.

Table C.1. Continued.

Karmn	Name	$P_{\mathrm{rot.,cl.}}$ [d]	Std. [d] [(a)]	GLS uncert. [d] [(a)]	$P_{\mathrm{rot.,lit.}}$ [d]	Ref.$_{\mathrm{lit.}}$	Reliability [(b)]	Match [(c)]	#Samples	Indicators [(d)]
J03463+262	HD 23453	10.07	0.01	0.01	16.40	Sh24	dubious	H	4	Hα, Ca IRT$_{\mathrm{b}}$, Ca IRT$_{\mathrm{a}}$, Ca IRT$_{\mathrm{c}}$
J04153-076	omi02 Eri C	137.41	3.97	1.34	8.56	Sh24	dubious	No	3	dLW (VIS), TiO 7048 Å, Paβ
J04290+219	BD+21 652	25.42	0.42	0.01	25.40	DA19	secure	D, YA	16	dLW (VIS), Ca IRT$_{\mathrm{c}}$, Ca IRT$_{\mathrm{b}}$, Hα, Ca IRT$_{\mathrm{a}}$, CCF-contrast (VIS), CCF-FWHM (VIS), Ca IRT$_{\mathrm{c}}$, dLW (NIR), RVs, Ca IRT$_{\mathrm{b}}$, NaD$_1$, CCF-FWHM (VIS), dLW (VIS), CCF-BVS (VIS), Ca IRT$_{\mathrm{a}}$
J04376+528	BD+52 857	16.31	0.04	0.01	15.47	Laf21	secure	D, YA	7	dLW (VIS), Ca IRT$_{\mathrm{c}}$, Ca IRT$_{\mathrm{a}}$, Ca IRT$_{\mathrm{b}}$, RVs, Paβ, Ca IRT$_{\mathrm{c}}$
J04588+498	BD+49 1280	19.21	0.05	0.01	17.46	Sh24	secure	D, YA	7	Ca IRT$_{\mathrm{a}}$, Ca IRT$_{\mathrm{c}}$, Ca IRT$_{\mathrm{b}}$, RVs, dLW (VIS), CCF-contrast (VIS), CCF-FWHM (VIS)
J05033-173	LP 776-046	…	…	…	…	…	…	…	…	…
J05127+196	GJ 192	…	…	…	32.70	Sh24	tentative	…	…	…
J05314-036	HD 36395	33.68	0.40	0.01	33.80	DA19	secure	D, YA	8	Ca IRT$_{\mathrm{c}}$, Ca IRT$_{\mathrm{b}}$, Ca IRT$_{\mathrm{a}}$, Hα, RVs, CCF-FWHM (VIS), Paβ, dLW (NIR)
J05365+113	V2689 Ori	11.79	0.02	0.01	11.75	Sh24	secure	D, YA	14	CCF-FWHM (VIS), Hα, RVs, Ca IRT$_{\mathrm{a}}$, dLW (NIR), Ca IRT$_{\mathrm{b}}$, Ca IRT$_{\mathrm{c}}$, NaD$_1$, CCF-BVS (VIS), TiO 7048 Å, dLW (VIS), CCF-contrast (VIS), NaD$_2$, Fe 8689 Å
J05415+534	HD 233153	…	…	…	17.39	Sh24	tentative	…	…	…
J05421+124	V1352 Ori	…	…	…	…	…	…	…	…	…
J06011+595	G 192-013	83.82	1.05	0.08	95.1	Don23	secure	D	5	TiO 7048 Å, RVs, CCF-contrast (VIS), dLW (VIS), NaD$_1$
J06024+498	G 192-015	…	…	…	105.00	DA19	secure	…	…	…
J06103+821	GJ 226	…	…	…	44.60	DA19	tentative	…	…	…
J06105-218	HD 42581	…	…	…	27.30	DA19	secure	…	…	…
J06371+175	HD 260655	…	…	…	37.50	Luq22	secure	…	…	…
J06396-210	LP 780-032	…	…	…	79.15	New18	tentative	…	…	…
J06548+332	Wolf 294	53.54	0.17	0.01	122.00	Sto20b	dubious	H	3	RVs, NaD$_1$, CCF-BVS (VIS)
J07274+052	Luyten's Star	95.12	0.79	0.04	93.50	SM17	dubious	D	4	RVs, dLW (VIS), Hα, dLW (VIS)
J07319+362N	BL Lyn	…	…	…	16.40	DA19	tentative	…	…	…
J07403-174	LP 783-002	…	…	…	…	…	…	…	…	…

References. DA19: Díez Alonso et al. (2019); SM23: Suárez Mascareño et al. (2023); SM18: Suárez Mascareño et al. (2023); Sh24: Shan et al. (2024); New18: Newton et al. (2018); Laf21: Lafarga et al. (2021); New16: Newton et al. (2016); Luq22: Luque et al. (2022); Sto20b: Stock et al. (2020b); SM17: Suárez Mascareño et al. (2017); Mor10: Morin et al. (2010); Diaz19: Díaz et al. (2019); Ste16: Stelzer et al. (2016); Luq18: Luque et al. (2018); SM15: Suárez Mascareño et al. (2015); TP19: Toledo-Padrón et al. (2019); Ama21: Amado et al. (2021); Wat06: Watson et al. (2006), Don23: Donati et al. (2023)

Notes. Rotation periods determined in this work are highlighted in bold font.

[(a)]Standard deviations and GLS uncertainties smaller then 0.00 d where conservatively set to 0.01 d [(b)]according to Shan et al. (2024) [(c)]YA: yearly alias match; DA: daily alias match; H: harmonic match; D: direct match [(d)]sorted by minimum FAP.

Table C.1. Continued.

Karmn	Name	$P_{\mathrm{rot,cl.}}$ [d]	Std. [d] [(a)]	GLS uncert. [d] [(a)]	$P_{\mathrm{rot,lit.}}$ [d]	Ref.$_{\mathrm{lit.}}$	Reliability [(b)]	Match [(c)]	#Samples	Indicators [(d)]
J07446+035	YZ CMi	2.78	0.01	0.01	2.78	Sh24	secure	D, YA	16	CCF-BVS (VIS), TiO 7048 Å, RVs, CCF-FWHM (VIS), CRX (VIS), TiO 8428 Å, CaH_3, CRX (NIR), VO 7434 Å, CCF-contrast (VIS), dLW (VIS), FeH WFB, RVs, CCF-BVS (VIS), CCF-FWHM (VIS), CRX (VIS)
J08161+013	GJ 2066	48.06	0.41	0.01	40.70	DA19	tentative	YA	5	Ca IRT_b, Hα, NaD_1, CCF-FWHM (VIS), RVs
J08413+594	LP 090-018	88.41	0.70	0.04	88.65	Laf21	secure	D	5	dLW (VIS), dLW (NIR), CCF-contrast (VIS), FeH WFB, Ca IRT_b
J08536-034	LP 666-009	…	…	…	0.46	Sh24	secure	…	…	…
J09144+526	HD 79211	16.67	0.03	0.01	16.88	Sh24	secure	D, YA	10	Ca IRT_c, Ca IRT_b, Ca IRT_a, CCF-FWHM (VIS), RVs, Hα, dLW (NIR), NaD_1, CCF-BVS (VIS), Paβ
J09411+132	Ross 85	…	…	…	…	…	…	…	…	…
J09425+700	GJ 360	…	…	…	21.00	DA19	tentative	…	…	…
J09428+700	GJ 362	24.57	0.03	0.01	24.33	Sh24	secure	D, YA	3	CCF-FWHM (VIS), NaD_1, TiO 7048 Å
J09561+627	BD+63 869	18.68	0.10	0.01	16.88	Sh24	secure	D, YA	7	RVs, NaD_1, CCF-FWHM (VIS), Paβ, CaH_3, TiO 7048 Å, RVs
J10122-037	AN Sex	21.42	0.01	0.01	23.00	Sh24	secure	D, YA	5	RVs, Ca IRT_c, Ca IRT_b, Ca IRT_a, Hα
J10289+008	BD+01 2447	…	…	…	31.72	Sh24	secure	…	…	…
J10482-113	LP 731-058	…	…	…	1.50	Mor10	secure	…	…	…
J10508+068	EE Leo	…	…	…	64.00	DA19	tentative	…	…	…
J10564+070	CN Leo	2.70	0.01	0.01	2.70	DA19	secure	D, YA	4	RVs, CRX (VIS), CCF-contrast (VIS), dLW (VIS)
J10584-107	LP 731-076	…	…	…	…	…	…	…	…	…
J11000+228	Ross 104	…	…	…	53.17	Sh24	secure	…	…	…
J11026+219	DS Leo	…	…	…	14.26	Sh24	secure	…	…	…
J11033+359	Lalande 21185	53.33	0.19	0.01	56.15	Diaz19	secure	D, YA	4	TiO 8428 Å, Hα, Ca IRT_a, FeH WFB
J11055+435	WX UMa	…	…	…	0.78	Mor10	secure	…	…	…
J11110+304W	HD 97101B	…	…	…	…	…	…	…	…	…
J11302+076	K2-18	44.62	1.85	0.12	36.40	DA19	secure	YA	4	Hα, Ca IRT_b, CaH_3, Ca IRT_c
J11417+427	Ross 1003	…	…	…	71.50	DA19	dubious	…	…	…

References. DA19: Díez Alonso et al. (2019); SM23: Suárez Mascareño et al. (2023); SM18: Suárez Mascareño et al. (2023); Sh24: Shan et al. (2024); New18: Newton et al. (2018); Laf21: Lafarga et al. (2021); New16: Newton et al. (2016); Luq22: Luque et al. (2022); Sto20b: Stock et al. (2020b); SM17: Suárez Mascareño et al. (2017); Mor10: Morin et al. (2010); Diaz19: Díaz et al. (2019); Ste16: Stelzer et al. (2016); Luq18: Luque et al. (2018); SM15: Suárez Mascareño et al. (2015); TP19: Toledo-Padrón et al. (2019); Ama21: Amado et al. (2021); Wat06: Watson et al. (2006), Don23: Donati et al. (2023)

Notes. Rotation periods determined in this work are highlighted in bold font.

[(a)]Standard deviations and GLS uncertainties smaller then 0.00 d where conservatively set to 0.01 d [(b)]according to Shan et al. (2024) [(c)]YA: yearly alias match; DA: daily alias match; H: harmonic match; D: direct match [(d)]sorted by minimum FAP.

Table C.1. Continued.

Karmn	Name	$P_{\mathrm{rot,cl.}}$ [d]	Std. [d] [(a)]	GLS uncert. [d] [(a)]	$P_{\mathrm{rot,lit.}}$ [d]	Ref.$_{\mathrm{lit.}}$	Reliability [(b)]	Match [(c)]	#Samples	Indicators [(d)]
J11474+667	1RXS J114728.8+664405	13.36	0.01	0.01	13.30	Sh24	secure	D, YA	10	RVs, TiO 7048 Å, TiO 8428 Å, CRX (VIS), CCF-contrast (VIS), CaH_3, CCF-FWHM (VIS), TiO 8858 Å, dLW (VIS), FeH WFB
J11476+786	GJ 445	…	…	…	…	…	…	…	…	…
J11477+008	FI Vir	…	…	…	112.80	Ste16	secure	…	…	…
J11509+483	GJ 1151	150.92	3.12	0.16	125.00	DA19	secure	YA	4	TiO 7048 Å, dLW (NIR), Hα, He 10830 Å
J11511+352	BD+36 2219	…	…	…	22.80	DA19	secure	…	…	…
J12100-150	LP 734-032	…	…	…	79.30	Sh24	tentative	…	…	…
J12123+544S	HD 238090	38.42	0.14	0.01	96.70	Sto20b	tentative	H	6	dLW (VIS), Ca IRT$_{\mathrm{c}}$, Ca IRT$_{\mathrm{b}}$, CCF-contrast (VIS), Ca IRT$_{\mathrm{a}}$, CCF-FWHM (VIS)
J12230+640	Ross 690	…	…	…	32.90	DA19	dubious	…	…	…
J12312+086	**BD+09 2636**	**21.42**	**0.07**	**0.01**	**…**	**This work**	**…**	**…**	**3**	**Hα, Ca IRT$_{\mathrm{c}}$, Ca IRT$_{\mathrm{a}}$**
J12479+097	Wolf 437	…	…	…	…	…	…	…	…	…
J13229+244	Ross 1020	136.46	2.59	0.95	95.00	Luq18	tentative	YA	3	TiO 7048 Å, CCF-FWHM (VIS), CCF-contrast (VIS)
J13299+102	BD+11 2576	30.78	0.08	0.01	30.00	SM17	secure	D, YA	6	Ca IRT$_{\mathrm{b}}$, Ca IRT$_{\mathrm{c}}$, CCF-contrast (VIS), Ca IRT$_{\mathrm{a}}$, CCF-FWHM (VIS), Hα
J13457+148	HD 119850	48.51	1.86	0.04	52.30	SM15	tentative	D, YA	10	Ca IRT$_{\mathrm{b}}$, Hα, Ca IRT$_{\mathrm{a}}$, Paβ, Ca IRT$_{\mathrm{c}}$, Ca IRT$_{\mathrm{b}}$, TiO 8428 Å, NaD_1, VO 7940 Å, Hα
J14257+236E	BD+24 2733B	…	…	…	17.60	DA19	dubious	…	…	…
J14257+236W	BD+24 2733A	…	…	…	111.00	DA19	tentative	…	…	…
J14307-086	**BD-07 3856**	**54.48**	**0.50**	**0.03**	**…**	**This work**	**…**	**…**	**6**	**Ca IRT$_{\mathrm{c}}$, dLW (VIS), Ca IRT$_{\mathrm{a}}$, CCF-contrast (VIS), Paβ, Ca IRT$_{\mathrm{b}}$**
J14321+081	LP 560-035	2.02	0.01	0.01	1.11	Sh24	secure	No	3	NaD_2, NaD_1, TiO 8428 Å
J14342-125	HN Lib	…	…	…	94.77	Sh24	secure	…	…	…
J15194-077	HO Lib	…	…	…	132.50	SM15	tentative	…	…	…
J15218+209	OT Ser	3.37	0.01	0.01	3.35	Sh24	secure	D, YA	6	CCF-contrast (VIS), RVs, CRX (VIS), dLW (VIS), VO 7940 Å, RVs
J16167+672N	EW Dra	36.24	0.09	0.01	40.40	Don23	tentative	D	5	NaD_1, NaD_2, Ca IRT$_{\mathrm{b}}$, CCF-FWHM (VIS), Hα
J16167+672S	HD 147379	22.06	0.07	0.01	22.00	Laf21	tentative	D, YA	7	Ca IRT$_{\mathrm{a}}$, Ca IRT$_{\mathrm{b}}$, RVs, Ca IRT$_{\mathrm{c}}$, CCF-BVS (VIS), CCF-FWHM (VIS), TiO 7048 Å
J16303-126	V2306 Oph	…	…	…	119.00	DA19	secure	…	…	…

References. DA19: Díez Alonso et al. (2019); SM23: Suárez Mascareño et al. (2023); SM18: Suárez Mascareño et al. (2023); Sh24: Shan et al. (2024); New18: Newton et al. (2018); Laf21: Lafarga et al. (2021); New16: Newton et al. (2016); Luq22: Luque et al. (2022); Sto20b: Stock et al. (2020b); SM17: Suárez Mascareño et al. (2017); Mor10: Morin et al. (2010); Diaz19: Díaz et al. (2019); Ste16: Stelzer et al. (2016); Luq18: Luque et al. (2018); SM15: Suárez Mascareño et al. (2015); TP19: Toledo-Padrón et al. (2019); Ama21: Amado et al. (2021); Wat06: Watson et al. (2006), Don23: Donati et al. (2023)

Notes. Rotation periods determined in this work are highlighted in bold font.

[(a)]Standard deviations and GLS uncertainties smaller then 0.00 d where conservatively set to 0.01 d [(b)]according to Shan et al. (2024) [(c)]YA: yearly alias match; DA: daily alias match; H: harmonic match; D: direct match [(d)]sorted by minimum FAP.

Table C.1. Continued.

Karmn	Name	$P_{\mathrm{rot,cl.}}$ [d]	Std. [d] [(a)]	GLS uncert. [d] [(a)]	$P_{\mathrm{rot,lit.}}$ [d]	Ref.$_{\mathrm{lit.}}$	Reliability [(b)]	Match [(c)]	#Samples	Indicators [(d)]
J16555-083	vB 8	11.19	0.02	0.01	1.09	Laf21	secure	DA	7	RVs, CCF-contrast (VIS), CCF-BVS (VIS), dLW (NIR), CCF-FWHM (VIS), CRX (NIR), CRX (VIS)
J16581+257	BD+25 3173	23.92	0.19	0.02	23.80	DA19	secure	D, YA	4	Ca IRT$_{\mathrm{b}}$, Ca IRT$_{\mathrm{c}}$, Ca IRT$_{\mathrm{a}}$, He 10830 Å
J17033+514	G 203-042	…	…	…	…	…	…	…	…	…
J17052-050	Wolf 636	…	…	…	50.20	DA19	tentative	…	…	…
J17115+384	Wolf 654	…	…	…	62.60	DA19	tentative	…	…	…
J17303+055	BD+05 3409	33.51	0.24	0.01	34.60	Sh24	secure	D, YA	10	Hα, Ca IRT$_{\mathrm{a}}$, CCF-FWHM (VIS), Ca IRT$_{\mathrm{b}}$, Ca IRT$_{\mathrm{c}}$, NaD$_2$, dLW (VIS), dLW (NIR), RVs, Paβ
J17378+185	BD+18 3421	37.24	0.78	0.01	35.02	Sh24	secure	D, YA	8	He 10830 Å, dLW (VIS), Ca IRT$_{\mathrm{c}}$, CCF-contrast (VIS), dLW (NIR), NaD$_1$, NaD$_2$, Ca IRT$_{\mathrm{a}}$
J17578+046	Barnard's Star	114.06	2.30	0.06	145.00	TP19	secure	YA	9	CaH$_3$, TiO 7048 Å, dLW (NIR), FeH WFB, TiO 7048 Å, CCF-BVS (VIS), TiO 8858 Å, TiO 8428 Å, CCF-FWHM (VIS)
J18027+375	GJ 1223	…	…	…	123.80	New16	tentative	…	…	…
J18051-030	HD 165222	34.16	0.21	0.01	127.80	SM15	dubious	No	4	dLW (NIR), Ca IRT$_{\mathrm{c}}$, NaD$_1$, Ca IRT$_{\mathrm{b}}$
J18165+048	G 140-51	…	…	…	…	…	…	…	…	…
J18174+483	TYC 3529-1437-1	16.00	0.07	0.01	15.83	Sh24	secure	D, YA	7	Ca IRT$_{\mathrm{b}}$, Ca IRT$_{\mathrm{a}}$, RVs, Ca IRT$_{\mathrm{c}}$, TiO 7048 Å, RVs, CCF-FWHM (VIS)
J18224+620	GJ 1227	…	…	…	…	…	…	…	…	…
J18346+401	LP 229-017	…	…	…	40.20	DA19	tentative	…	…	…
J18409-133	BD-13 5069	26.05	0.08	0.01	28.23	Sh24	tentative	D, YA	4	dLW (VIS), Ca IRT$_{\mathrm{c}}$, CCF-contrast (VIS), Ca IRT$_{\mathrm{a}}$
J18482+076	G 141-036	…	…	…	2.76	DA19	secure	…	…	…
J19072+208	HD 349726	…	…	…	3.80	DA19	dubious	…	…	…
J19169+051N	V1428 Aql	50.43	1.17	0.08	46.00	DA19	secure	D, YA	10	Ca IRT$_{\mathrm{b}}$, Ca IRT$_{\mathrm{a}}$, Paβ, NaD$_1$, Ca IRT$_{\mathrm{c}}$, TiO 7048 Å, CaH$_3$, CCF-FWHM (VIS), TiO 8428 Å, RVs
J19169+051S	V1298 Aql	…	…	…	23.60	DA19	dubious	…	…	…
J19255+096	LSPM J1925+0938	…	…	…	…	…	…	…	…	…

References. DA19: Díez Alonso et al. (2019); SM23: Suárez Mascareño et al. (2023); SM18: Suárez Mascareño et al. (2023); Sh24: Shan et al. (2024); New18: Newton et al. (2018); Laf21: Lafarga et al. (2021); New16: Newton et al. (2016); Luq22: Luque et al. (2022); Sto20b: Stock et al. (2020b); SM17: Suárez Mascareño et al. (2017); Mor10: Morin et al. (2010); Diaz19: Díaz et al. (2019); Ste16: Stelzer et al. (2016); Luq18: Luque et al. (2018); SM15: Suárez Mascareño et al. (2015); TP19: Toledo-Padrón et al. (2019); Ama21: Amado et al. (2021); Wat06: Watson et al. (2006), Don23: Donati et al. (2023)

Notes. Rotation periods determined in this work are highlighted in bold font.

[(a)]Standard deviations and GLS uncertainties smaller then 0.00 d where conservatively set to 0.01 d [(b)]according to Shan et al. (2024) [(c)]YA: yearly alias match; DA: daily alias match; H: harmonic match; D: direct match [(d)]sorted by minimum FAP.

Table C.1. Continued.

Karmn	Name	$P_{\mathrm{rot,cl.}}$ [d]	Std. [d] [a]	GLS uncert. [d] [a]	$P_{\mathrm{rot,lit.}}$ [d]	Ref.$_{\mathrm{lit.}}$	Reliability [b]	Match [c]	#Samples	Indicators [d]
J19346+045	BD+04 4157	21.76	0.06	0.01	21.79	Sh24	secure	D, YA	10	Ca IRT$_{\mathrm{c}}$, Ca IRT$_{\mathrm{b}}$, dLW (NIR), Ca IRT$_{\mathrm{a}}$, dLW (VIS), CCF-FWHM (VIS), Hα, Paβ, NaD$_2$, CCF-BVS (VIS)
J20260+585	Wolf 1069	156.30	8.68	0.46	57.70	DA19	dubious	No	7	CCF-BVS (VIS), FeH WFB, TiO 7048 Å, He 10830 Å, CaH$_3$, He I D$_3$, CCF-FWHM (VIS)
J20305+654	GJ 793	…	…	…	32.80	DA19	secure	…	…	…
J20336+617	GJ 1254	…	…	…	12.60	DA19	tentative	…	…	…
J20450+444	BD+44 3567	39.23	0.10	0.01	39.12	Sh24	tentative	D, YA	4	NaD$_1$, Ca IRT$_{\mathrm{c}}$, CCF-FWHM (VIS), Hα
J20525-169	LP 816-060	…	…	…	67.60	DA19	dubious	…	…	…
J20533+621	**HD 199305**	**159.61**	**4.53**	**0.52**	**…**	**This work**	**…**	**…**	**6**	**He 10830 Å, Ca IRT$_{\mathrm{c}}$, Ca IRT$_{\mathrm{b}}$, dLW (VIS), Ca IRT$_{\mathrm{a}}$, CCF-contrast (VIS)**
J20556-140S	GJ 810 B	27.34	0.01	0.01	134.60	New18	tentative	No	4	dLW (VIS), NaD$_2$, NaD$_1$, CCF-contrast (VIS)
J21164+025	LSPM J2116+0234	44.15	0.49	0.03	42.68	Sh24	secure	D, YA	8	TiO 7048 Å, RVs, dLW (NIR), CCF-FWHM (VIS), NaD$_1$, Ca IRT$_{\mathrm{a}}$, CaH$_3$, Ca IRT$_{\mathrm{c}}$
J21221+229	TYC 2187-512-1	39.75	0.31	0.01	38.40	Sh24	secure	D, YA	14	dLW (NIR), Ca IRT$_{\mathrm{b}}$, Ca IRT$_{\mathrm{c}}$, Ca IRT$_{\mathrm{a}}$, CCF-FWHM (VIS), Hα, NaD$_1$, RVs, NaD$_2$, dLW (VIS), CaH$_3$, He 10830 Å, CCF-contrast (VIS), CRX (VIS)
J21348+515	Wolf 926	56.77	0.33	0.04	54.30	DA19	secure	D, YA	3	He 10830 Å, Ca IRT$_{\mathrm{b}}$, FeH WFB
J21463+382	LSPM J2146+3813	…	…	…	…	…	…	…	…	…
J21466+668	G 264-012	15.17	0.04	0.01	100.00	Ama21	tentative	No	3	CaH$_3$, dLW (VIS), Ca IRT$_{\mathrm{c}}$
J22021+014	BD+00 4810	…	…	…	29.50	DA19	dubious	…	…	…
J22057+656	G 264-18 A	…	…	…	120.50	Laf21	tentative	…	…	…
J22096-046	BD-05 5715	…	…	…	39.20	SM15	secure	…	…	…
J22115+184	Ross 271	34.23	0.16	0.01	36.30	DA19	secure	D, YA	8	CCF-FWHM (VIS), Ca IRT$_{\mathrm{c}}$, NaD$_1$, NaD$_2$, Ca IRT$_{\mathrm{b}}$, RVs, dLW (NIR), Hα
J22125+085	Wolf 1014	…	…	…	…	…	…	…	…	…
J22137-176	LP 819-052	…	…	…	116.40	Ste16	tentative	…	…	…
J22252+594	G 232-070	…	…	…	64.60	DA19	secure	…	…	…

References. DA19: Díez Alonso et al. (2019); SM23: Suárez Mascareño et al. (2023); SM18: Suárez Mascareño et al. (2023); Sh24: Shan et al. (2024); New18: Newton et al. (2018); Laf21: Lafarga et al. (2021); New16: Newton et al. (2016); Luq22: Luque et al. (2022); Sto20b: Stock et al. (2020b); SM17: Suárez Mascareño et al. (2017); Mor10: Morin et al. (2010); Diaz19: Díaz et al. (2019); Ste16: Stelzer et al. (2016); Luq18: Luque et al. (2018); SM15: Suárez Mascareño et al. (2015); TP19: Toledo-Padrón et al. (2019); Ama21: Amado et al. (2021); Wat06: Watson et al. (2006), Don23: Donati et al. (2023)

Notes. Rotation periods determined in this work are highlighted in bold font.

[a]Standard deviations and GLS uncertainties smaller then 0.00 d where conservatively set to 0.01 d [b]according to Shan et al. (2024) [c]YA: yearly alias match; DA: daily alias match; H: harmonic match; D: direct match [d]sorted by minimum FAP.

Table C.1. Continued.

Karmn	Name	$P_{\mathrm{rot,cl.}}$ [d]	Std. [d] [(a)]	GLS uncert. [d] [(a)]	$P_{\mathrm{rot,lit.}}$ [d]	Ref.$_{\mathrm{lit.}}$	Reliability [(b)]	Match [(c)]	#Samples	Indicators [(d)]
J22330+093	BD+08 4887	37.66	0.11	0.01	37.80	Sh24	secure	D, YA	9	Ca IRT$_{\mathrm{c}}$, Hα, RVs, Ca IRT$_{\mathrm{a}}$, Ca IRT$_{\mathrm{b}}$, dLW (NIR), NaD$_1$, TiO 8858 Å, CCF-contrast (VIS)
J22468+443	EV Lac	4.37	0.01	0.01	4.35	Sh24	secure	D, YA	16	RVs, dLW (VIS), CCF-FWHM (VIS), TiO 7048 Å, CCF-contrast (VIS), dLW (NIR), Hα, CCF-BVS (VIS), CaH$_3$, Ca IRT$_{\mathrm{c}}$, Ca IRT$_{\mathrm{b}}$, CRX (VIS), NaD$_1$, Ca IRT$_{\mathrm{a}}$, TiO 8428 Å, NaD$_2$
J22503-070	BD-07 5871	…	…	…	…	…	…	…	…	…
J22532-142	IL Aqr	51.39	0.42	0.02	81.00	DA19	secure	H	3	Paβ, TiO 8428 Å, CCF-FWHM (VIS)
J22565+165	HD 216899	39.85	0.50	0.01	39.50	DA19	secure	D, YA	25	dLW (VIS), Ca IRT$_{\mathrm{b}}$, Ca IRT$_{\mathrm{c}}$, RVs, Ca IRT$_{\mathrm{a}}$, dLW (NIR), CCF-contrast (VIS), NaD$_2$, CCF-FWHM (VIS), dLW (VIS), Ca IRT$_{\mathrm{b}}$, Ca IRT$_{\mathrm{c}}$, Paβ, Ca IRT$_{\mathrm{a}}$, NaD$_1$, Hα, He 10830 Å, FeH WFB, Paβ, TiO 8858 Å, CCF-FWHM (VIS), CCF-contrast (VIS), dLW (NIR), TiO 8428 Å, CRX (VIS)
J23216+172	LP 462-027	34.46	0.38	0.01	74.70	DA19	secure	H	4	CCF-contrast (VIS), dLW (VIS), CCF-FWHM (VIS), VO 7434 Å
J23245+578	BD+57 2735	…	…	…	36.48	Sh24	secure	…	…	…
J23351-023	GJ 1286	…	…	…	88.92	New18	dubious	…	…	…
J23381-162	G 273-093	47.21	0.66	0.02	61.66	Wat06	dubious	YA	3	Paβ, TiO 8858 Å, CaH$_3$
J23419+441	HH And	2.07	0.01	0.01	106.00	DA19	secure	No	3	NaD$_2$, Hα, NaD$_1$
J23492+024	BR Psc	50.83	0.35	0.01	49.90	SM18	secure	D, YA	8	dLW (NIR), CCF-FWHM (VIS), TiO 7048 Å, CaH$_3$, TiO 8428 Å, Paβ, NaD$_1$, FeH WFB
J23505-095	LP 763-012	…	…	…	…	…	…	…	…	…

References. DA19: Díez Alonso et al. (2019); SM23: Suárez Mascareño et al. (2023); SM18: Suárez Mascareño et al. (2023); Sh24: Shan et al. (2024); New18: Newton et al. (2018); Laf21: Lafarga et al. (2021); New16: Newton et al. (2016); Luq22: Luque et al. (2022); Sto20b: Stock et al. (2020b); SM17: Suárez Mascareño et al. (2017); Mor10: Morin et al. (2010); Diaz19: Díaz et al. (2019); Ste16: Stelzer et al. (2016); Luq18: Luque et al. (2018); SM15: Suárez Mascareño et al. (2015); TP19: Toledo-Padrón et al. (2019); Ama21: Amado et al. (2021); Wat06: Watson et al. (2006), Don23: Donati et al. (2023)

Notes. Rotation periods determined in this work are highlighted in bold font.

[(a)]Standard deviations and GLS uncertainties smaller then 0.00 d where conservatively set to 0.01 d [(b)]according to Shan et al. (2024) [(c)]YA: yearly alias match; DA: daily alias match; H: harmonic match; D: direct match [(d)]sorted by minimum FAP.

Table C.2. Long term signals in the data. Signals with periods that are unresolved are reported with the timespan of the data as minimum values.

Karmn	Name	$P_{\mathrm{lt.,cl.}}$ [d]	$P_{\mathrm{lt.,Fu23}}$ [d]	$P_{\mathrm{rot.,cl.}}$ [d]	$P_{\mathrm{rot.,lit.}}$ [d]	#Samples	timespan [d]	RV rms [m s^{-1}]	Indicators[(a)]
J00183+440	GX And	468	...	41.13	45.00	3	1502.04	3.03	TiO 7048 Å, Ca IRT$_b$, CCF-FWHM (VIS)
J00183+440	GX And	>1502	...	41.13	45.00	3	1502.04	3.03	CCF-FWHM (VIS), CRX (VIS), NaD$_1$
J00184+440	GQ And	>1445	...	108.20	...	13	1445.99	2.51	CRX (NIR), NaD$_2$, CCF-FWHM (VIS), CRX (VIS), RVs, NaD$_1$, Hα, dLW (VIS), TiO 8428 Å, CCF-contrast (VIS), CaH$_3$, dLW (NIR), Paβ
J00184+440	GQ And	304	...	108.20	...	6	1445.99	2.51	RVs, dLW (NIR), CCF-FWHM (VIS), VO 7940 Å, Fe 8689 Å, FeH WFB
J01026+623	BD+61 195	>779	...	18.91	18.82	7	779.99	5.53	CCF-contrast (VIS), dLW (VIS), dLW (NIR), Ca IRT$_b$, Hα, Ca IRT$_a$, CaH$_3$
J02123+035	BD+02 348	>1563	...	...	17.11	3	1563.67	2.03	He 10830 Å, Ca IRT$_b$, CRX (VIS)
J02222+478	BD+47 612	>718	...	31.13	29.50	3	719.00	4.70	NaD$_2$, Hα, NaD$_1$
J02530+168	Teegarden's Star	>1385	...	98.05	97.56	6	1385.35	2.98	CCF-contrast (VIS), CCF-FWHM (VIS), NaD$_1$, FeH WFB, dLW (NIR), NaD$_2$
J04290+219	BD+21 652	>749	657.00	25.42	25.40	8	749.03	4.55	CCF-contrast (VIS), Hα, NaD$_1$, dLW (VIS), Ca IRT$_c$, Ca IRT$_b$, Ca IRT$_a$, NaD$_2$
J04588+498	BD+49 1280	>1464	...	19.21	17.46	4	1464.92	8.95	CCF-contrast (VIS), Ca IRT$_c$, CCF-FWHM (VIS), NaD$_1$
J06105-218	HD 42581	>1421	...	...	27.30	8	1421.09	5.09	Ca IRT$_b$, Ca IRT$_c$, Ca IRT$_a$, Hα, CCF-FWHM (VIS), dLW (VIS), CCF-contrast (VIS), NaD$_1$
J06371+175	HD 260655	741	...	...	37.50	4	2310.80	3.41	He 10830 Å, Hα, CCF-FWHM (VIS), NaD$_1$
J06371+175	HD 260655	>2310	...	...	37.50	3	2310.80	3.41	CCF-contrast (VIS), dLW (VIS), NaD$_2$
J06548+332	Wolf 294	646	...	53.54	122.00	6	2498.02	3.71	NaD$_1$, Ca IRT$_b$, TiO 7048 Å, FeH WFB, Ca IRT$_a$, CCF-FWHM (VIS)
J06548+332	Wolf 294	>2498	...	53.54	122.00	3	2498.02	3.71	Hα, dLW (NIR), CRX (NIR)
J07274+052	Luyten's Star	1092	1022.00	95.12	93.50	8	2498.09	3.17	Hα, RVs, Ca IRT$_c$, RVs, CRX (VIS), CCF-contrast (VIS), He 10830 Å, dLW (VIS)
J07274+052	Luyten's Star	293	1022.00	95.12	93.50	3	2498.09	3.17	TiO 8428 Å, CRX (VIS), NaD$_1$
J07274+052	Luyten's Star	551	1022.00	95.12	93.50	3	2498.09	3.17	RVs, He I D$_3$, RVs
J10289+008	BD+01 2447	>1620	...	...	31.72	3	1620.71	2.36	Hα, Ca IRT$_c$, Ca IRT$_b$
J10564+070	CN Leo	>815	...	2.70	2.70	3	815.72	6.08	dLW (NIR), dLW (VIS), CCF-contrast (VIS)
J11033+359	Lalande 21185	>2498	...	53.33	56.15	17	2498.06	3.86	NaD$_2$, Hα, NaD$_1$, NaD$_2$, dLW (VIS), CCF-contrast (VIS), He 10830 Å, NaD$_1$, dLW (NIR), Hα, FeH WFB, Hα, CCF-contrast (VIS), CaH$_2$, NaD$_2$, NaD$_1$, CaH$_3$
J11033+359	Lalande 21185	536	...	53.33	56.15	15	2498.06	3.86	NaD$_2$, He 10830 Å, CaH$_3$, dLW (VIS), dLW (NIR), Hα, CCF-contrast (VIS), dLW (NIR), CCF-FWHM (VIS), NaD$_1$, He 10830 Å, Hα, Ca IRT$_c$, VO 7940 Å, CRX (NIR)
J11033+359	Lalande 21185	318	...	53.33	56.15	3	2498.06	3.86	VO 7940 Å, NaD$_1$, NaD$_1$
J11417+427	Ross 1003	>1193	...	...	71.50	4	1193.84	25.16	RVs, FeH WFB, Hα, CCF-FWHM (VIS)

Notes. [(a)] sorted by minimum FAP

Table C.2. continued.

Karmn	Name	$P_{\mathrm{lt.,cl.}}$ [d]	$P_{\mathrm{lt.,Fu23}}$ [d]	$P_{\mathrm{rot.,cl.}}$ [d]	$P_{\mathrm{rot.,lit.}}$ [d]	#Samples	timespan [d]	RV rms [m s^{-1}]	Indicators[(a)]
J11509+483	GJ 1151	958	...	150.92	125.00	6	2356.70	4.09	CCF-FWHM (VIS), Hα, dLW (NIR), TiO 8428 Å, Ca IRT$_b$, CaH$_3$
J12123+544S	HD 238090	535	547.50	38.42	96.70	8	1192.92	3.31	Paβ, Ca IRT$_b$, Ca IRT$_a$, He 10830 Å, Ca IRT$_c$, NaD$_2$, CCF-FWHM (VIS), NaD$_1$
J13299+102	BD+11 2576	1099	547.50	30.78	30.00	24	2384.60	3.62	Ca IRT$_b$, Ca IRT$_c$, dLW (VIS), Ca IRT$_a$, NaD$_1$, CCF-contrast (VIS), CCF-FWHM (VIS), NaD$_2$, dLW (NIR), Ca IRT$_c$, RVs, Ca IRT$_b$, FeH WFB, Paβ, Ca IRT$_c$, CRX (NIR), TiO 7048 Å, Ca IRT$_c$, dLW (VIS), Ca IRT$_a$, Paβ, TiO 8858 Å, Ca IRT$_b$, VO 7940 Å
J13299+102	BD+11 2576	280	547.50	30.78	30.00	4	2384.60	3.62	Hα, Ca IRT$_b$, Ca IRT$_a$, NaD$_2$
J13457+148	HD 119850	262	...	48.51	52.30	7	815.88	3.57	CCF-FWHM (VIS), RVs, dLW (VIS), Hα, Ca IRT$_b$, CaH$_2$, NaD$_1$
J13457+148	HD 119850	>815	...	48.51	52.30	6	815.88	3.57	Hα, CCF-contrast (VIS), dLW (NIR), He 10830 Å, RVs, NaD$_2$
J14257+236W	BD+24 2733A	208	438.00	...	111.00	5	1290.66	4.02	Paβ, dLW (NIR), Ca IRT$_b$, Ca IRT$_c$, Ca IRT$_a$
J16167+672S	HD 147379	>1634	...	22.06	22.00	6	1634.72	5.84	CCF-FWHM (VIS), Ca IRT$_b$, Ca IRT$_c$, Ca IRT$_a$, dLW (NIR), dLW (VIS)
J16167+672S	HD 147379	203	...	22.06	22.00	5	1634.72	5.84	Ca IRT$_b$, CCF-contrast (VIS), Ca IRT$_c$, dLW (VIS), CCF-FWHM (VIS)
J16167+672S	HD 147379	502	...	22.06	22.00	4	1634.72	5.84	Paβ, Ca IRT$_c$, Ca IRT$_b$, Hα
J16167+672S	HD 147379	235	...	22.06	22.00	3	1634.72	5.84	VO 7940 Å, Ca IRT$_a$, CCF-FWHM (VIS)
J17303+055	BD+05 3409	>904	...	33.51	34.60	3	904.65	3.40	Ca IRT$_c$, Ca IRT$_a$, CCF-FWHM (VIS)
J17578+046	Barnard's Star	>2463	...	114.06	145.00	12	2463.51	2.80	CCF-FWHM (VIS), dLW (NIR), CaH$_3$, dLW (VIS), CCF-contrast (VIS), dLW (NIR), TiO 7048 Å, TiO 8428 Å, Fe 8689 Å, RVs, CRX (NIR), Ca IRT$_c$
J17578+046	Barnard's Star	751	...	114.06	145.00	12	2463.51	2.80	dLW (NIR), dLW (NIR), dLW (VIS), TiO 7048 Å, CCF-contrast (VIS), CCF-FWHM (VIS), TiO 7048 Å, FeH WFB, CCF-FWHM (VIS), He 10830 Å, dLW (NIR), Hα
J17578+046	Barnard's Star	268	...	114.06	145.00	5	2463.51	2.80	Fe 8689 Å, CaH$_3$, CRX (VIS), Paβ, TiO 8428 Å
J17578+046	Barnard's Star	459	...	114.06	145.00	3	2463.51	2.80	He 10830 Å, CCF-FWHM (VIS), dLW (NIR)
J18224+620	GJ 1227	490	...	...	...	3	1608.73	3.52	CCF-contrast (VIS), TiO 7048 Å, dLW (VIS)
J18346+401	LP 229-017	>1759	1460.00	...	40.20	3	1759.09	3.31	Ca IRT$_b$, Ca IRT$_a$, CCF-contrast (VIS)
J19169+051N	V1428 Aql	241	...	50.43	46.00	4	621.52	3.11	TiO 7048 Å, TiO 8428 Å, FeH WFB, He 10830 Å
J19169+051N	V1428 Aql	>621	...	50.43	46.00	3	621.52	3.11	CCF-FWHM (VIS), Ca IRT$_c$, dLW (VIS)
J20260+585	Wolf 1069	>1453	...	156.30	57.70	17	1453.99	2.94	CaH$_3$, Hα, Ca IRT$_b$, TiO 7048 Å, NaD$_1$, NaD$_2$, dLW (NIR), CCF-FWHM (VIS), TiO 7048 Å, RVs, CCF-contrast (VIS), dLW (VIS), VO 7940 Å, CRX (VIS), VO 7434 Å, FeH WFB, Hα
J20533+621	HD 199305	>1400	...	159.61	...	3	1400.98	2.85	dLW (NIR), Hα, NaD$_1$

Notes. [(a)] sorted by minimum FAP

Table C.2. continued.

Karmn	Name	$P_{\mathrm{lt.,cl.}}$ [d]	$P_{\mathrm{lt.,Fu23}}$ [d]	$P_{\mathrm{rot.,cl.}}$ [d]	$P_{\mathrm{rot.,lit.}}$ [d]	#Samples	timespan [d]	RV rms [m s^{-1}]	Indicators[(a)]
J21164+025	LSPM J2116+0234	>1036	...	44.15	42.68	3	1036.03	5.24	CRX (VIS), CCF-contrast (VIS), TiO 8858 Å
J21466+668	G 264-012	>1306	...	15.17	100.00	4	1306.65	4.39	Ca IRT$_b$, CaH$_3$, Hα, FeH WFB
J22057+656	G 264-18 A	>939	3650.00	...	120.50	4	939.69	3.87	TiO 8428 Å, Ca IRT$_b$, Hα, Ca IRT$_a$
J22125+085	Wolf 1014	1092	...	...	...	3	2298.73	8.10	RVs, CaH$_3$, Ca IRT$_c$
J22137-176	LP 819-052	>781	...	...	116.40	3	781.82	7.64	RVs, CRX (NIR), CaH$_3$
J22330+093	BD+08 4887	1115	1131.50	37.66	37.80	6	2248.89	3.77	Hα, Ca IRT$_a$, Ca IRT$_c$, Ca IRT$_b$, CCF-FWHM (VIS), CaH$_3$
J22330+093	BD+08 4887	320	1131.50	37.66	37.80	3	2248.89	3.77	Ca IRT$_b$, Ca IRT$_c$, Ca IRT$_a$
J22532-142	IL Aqr	>1261	...	51.39	81.00	10	1261.67	168.60	dLW (VIS), CCF-contrast (VIS), CaH$_3$, TiO 7048 Å, Ca IRT$_b$, CaH$_3$, VO 7940 Å, TiO 8858 Å, CRX (VIS), Ca IRT$_a$
J22565+165	HD 216899	>2499	1971.00	39.85	39.50	21	2499.96	3.64	dLW (VIS), CCF-contrast (VIS), Ca IRT$_c$, NaD$_1$, Ca IRT$_a$, Hα, dLW (NIR), Ca IRT$_b$, NaD$_2$, RVs, He 10830 Å, CCF-FWHM (VIS), CRX (NIR), He 10830 Å, NaD$_1$, FeH WFB, Paβ, Hα, TiO 8428 Å, Ca IRT$_a$, Ca IRT$_b$
J22565+165	HD 216899	577	1971.00	39.85	39.50	10	2499.96	3.64	CaH$_3$, Hα, TiO 7048 Å, Ca IRT$_b$, Ca IRT$_c$, Ca IRT$_a$, NaD$_2$, CCF-FWHM (VIS), dLW (NIR), Paβ
J22565+165	HD 216899	321	1971.00	39.85	39.50	6	2499.96	3.64	TiO 7048 Å, RVs, dLW (NIR), CCF-contrast (VIS), VO 7940 Å, CaH$_3$
J22565+165	HD 216899	252	1971.00	39.85	39.50	3	2499.96	3.64	TiO 7048 Å, CCF-contrast (VIS), dLW (VIS)
J23216+172	LP 462-027	248	...	34.46	74.70	4	1186.77	2.98	CCF-contrast (VIS), dLW (VIS), TiO 7048 Å, VO 7434 Å
J23419+441	HH And	>1383	...	2.07	106.00	8	1383.13	2.61	CCF-contrast (VIS), TiO 7048 Å, Hα, dLW (VIS), VO 7940 Å, NaD$_1$, Ca IRT$_b$, Ca IRT$_a$
J23492+024	BR Psc	>2498	...	50.83	49.90	12	2498.25	2.41	Hα, dLW (NIR), RVs, dLW (VIS), Ca IRT$_c$, NaD$_1$, CaH$_3$, TiO 7048 Å, Ca IRT$_b$, CRX (NIR), Ca IRT$_a$, TiO 8858 Å

Notes. [(a)] sorted by minimum FAP

Appendix D: Clustering diagrams of the rotation periods detected in this work

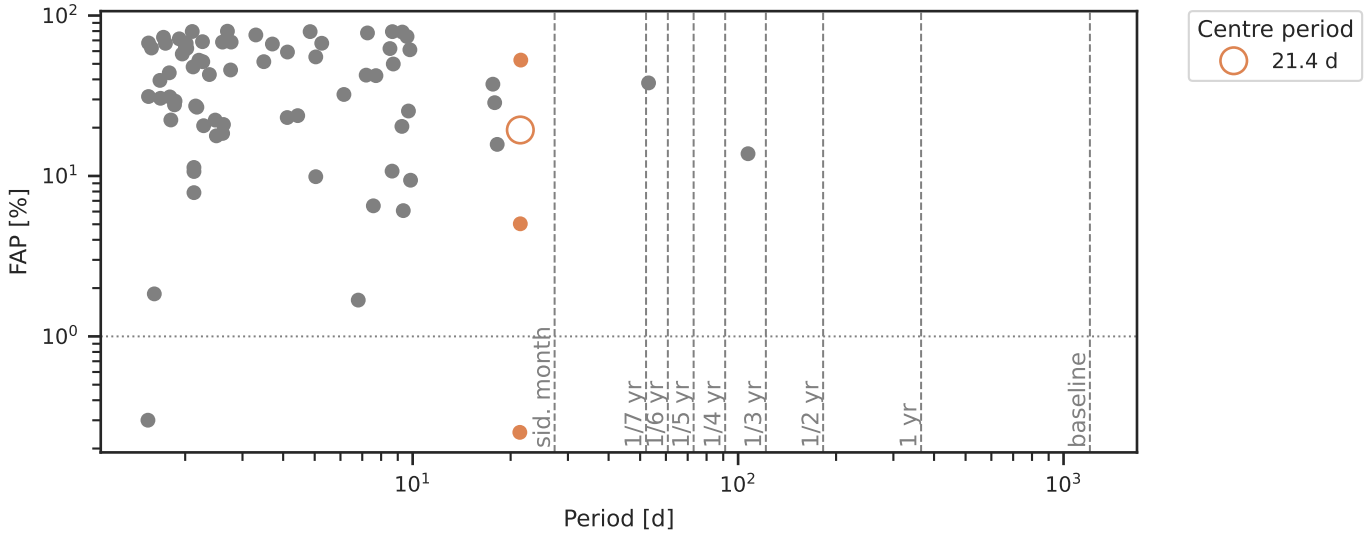

Fig. D.1. Results of the clustering algorithm for BD+09 2636 using the pre-whitening method with the yearly aliases removed. The FAP of 1 % is marked by the grey horizontal dotted line and the grey vertical dashed lines show different periods of interest. The error bars of the data points correspond to the peak width in the GLS.

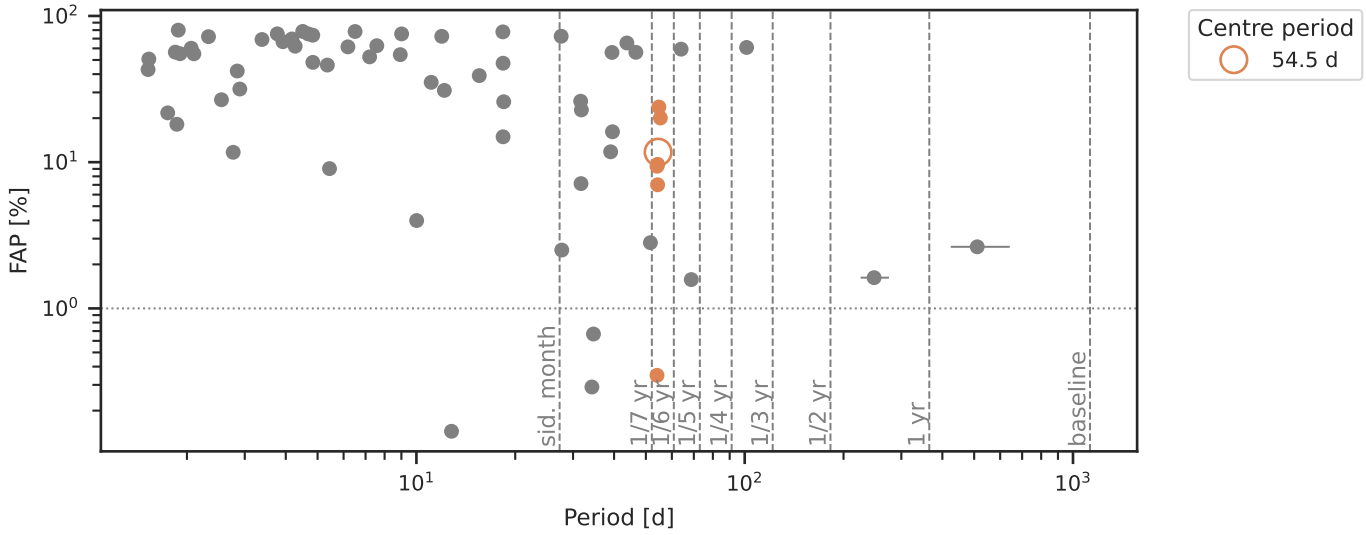

Fig. D.2. Same as Fig. D.1, but for BD-07 3856.

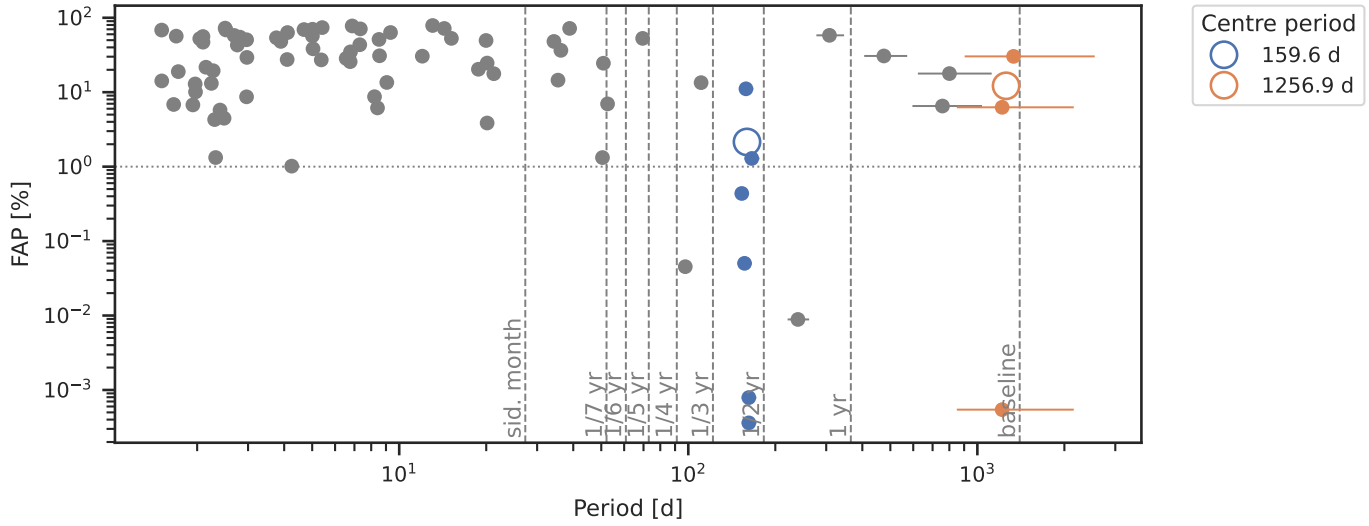

Fig. D.3. Same as Fig. D.1, but for HD 199305.